INTEGRATED MULTI-MEDIA PLATFORM FOR HYBRID 3D PRINTING

A Thesis
Presented to
The Academic Faculty

by

Conner K. Dunn

In Partial Fulfillment
of the Requirements for the Degree
Master of Science in the
George W. Woodruff School of Mechanical Engineering

Georgia Institute of Technology
August 2017

INTEGRATED MULTI-MEDIA PLATFORM FOR HYBRID 3D PRINTING

Approved by:

Dr. H. Jerry Qi, Advisor
George W. Woodruff School of Mechanical Engineering
Georgia Institute of Technology

Dr. Suman Das
George W. Woodruff School of Mechanical Engineering
Georgia Institute of Technology

Dr. Shuman Xia
George W. Woodruff School of Mechanical Engineering
Georgia Institute of Technology

Date Approved: July 19, 2017

ACKNOWLEDGEMENTS

First and foremost, I would like to thank my advisor, Dr. H. Jerry Qi, for his guidance and trust in me throughout the years. I am forever grateful for the opportunities that he has presented me with. His time and effort spent mentoring me during various parts of my academic career will not be forgotten.

I would also like to thank all past and current group members of the Mechanics of Soft Materials and 3D Printing Laboratory, for their friendship, guidance and advice over the years. Without our collaboration and fruitful conversations, I would not have been able to complete this thesis.

I would like to thank Dr. Suman Das and Dr. Shuman Xia for agreeing to serve on my thesis committee despite their extremely busy schedules.

Lastly, I would like to think my family and friends that have always been there to support me throughout the years. I would not be where I am today without them.

TABLE OF CONTENTS

ACKNOWLEDGEMENTS iii

LIST OF FIGURES vi

LIST OF SYMBOLS AND ABBREVIATIONS ix

SUMMARY x

CHAPTER 1.
INTRODUCTION 1
1.1 Additive Manufacturing Methods 3
1.1.1 Fused Deposition Modelling 3
1.1.2 Photopolymer Inkjet Printing 5
1.1.3 Aerosol Jetting 6
1.1.4 Direct Ink Writing 7
1.2 Motivation and Objective 8
1.3 Outline 9
CHAPTER 2.
INTEGRATED MULTI-MEDIA PLATFORM 11
2.1 Layout and Design 11
2.2 Motion System 12
2.3 Optomec Print Engine 14
2.4 Xenon Photonic Curing 17
2.5 Extrusion Based Technologies 19
2.5.1 Fused Deposition Modelling 20
2.5.2 Direct Ink Writing 24
2.6 Photopolymer Inkjet Printing 25
2.7 Robotic Pick and Place 30
2.8 Software and Firmware 31
2.9 Printing Methods 32
2.10 Summary 34
CHAPTER 3.
THERMAL CURE EFFECTS OF SILVER NANOPARTICLE INK 36
3.1 Materials and Methods 37
3.1.1 Materials 37
3.1.2 DIW Setup 37
3.1.3 Thermal Curing 38
3.1.4 Measurement of Cross Sectional Area 38
3.1.5 Stress-Strain and Cyclic Testing 39
3.1.6 Resistivity 40
3.1.7 Other Characterization Methods 40
3.2 Effect of Thermal Curing Conditions 41
3.2.1 Mass Loss During Curing 41
3.2.2 In Situ Resistance Change During Curing 42

3.2.3 Microstructure Characterization 45
3.2.4 Electro-Mechanical Properties 47
3.2.5 Conductivity 48
3.2.6 Young's Moduli 51
3.2.7 Yield Strain 53
3.2.8 Elongation 54
3.2.9 Repeatability 55
3.3 Summary 60
CHAPTER 4.
APPLICATIONS OF HYBRID 3D PRINTING 61
4.1 Stretchable Electronics 61
4.1.1 Stretchable Ribbon Cable 62
4.1.2 Soft Strain Sensor 63
4.2 Mechanically Heterogenous Structures 66
4.3 Soft Robotics 74
4.4 Smart Structures 78
4.4.1 SMP Recovery 78
4.5 Embedded Electronics 80
4.5.1 Digital LED Lamp 80
4.5.2 Fully Printed Capacitor 83
4.6 Summary 86
CHAPTER 5.
SUMMARY AND CONCLUSIONS 87
5.1 Contributions 87
5.2 Future Work 88

REFERENCES 89

LIST OF FIGURES

Figure 1. Simplified Schematic of Fused Deposition Modeling..... 4
Figure 2. Photopolymer Inkjet Printing simplified schematic..... 5
Figure 3. Simplified Schematic of Aerosol Jetting..... 6
Figure 4. Simplified Schematic of Direct Ink Writing..... 7
Figure 5. CAD representation of Multi-Media Hybrid 3D Printer..... 12
Figure 6. Operational workflow schematic of Multi-Media Hybrid 3D printer..... 14
Figure 7. Schematic diagram of Aerosol Jetting based printing system..... 15
Figure 8. Schematic of Optomec Aerosol Jetting operation..... 16
Figure 9. Microscopic Images of Aerosol Jetting printed silver lines..... 17
Figure 10. Schematic of Xenon Photonic Curing operation..... 18
Figure 11. In-Situ resistance measurements of silver ink being cured by Xenon Photonic Curing System..... 19
Figure 12. Schematic of FDM printhead operation..... 22
Figure 13. Temperature response of hotend under PID control..... 24
Figure 14. Schematic of DIW operation..... 25
Figure 15. Schematic Diagram of Photopolymer Inkjet Printing operation..... 27
Figure 16. Layer thickness as a function of inkjet resolution..... 28
Figure 17. CAD designs and corresponding inkjet printed parts..... 29
Figure 18. Robotic arm Pick and Place vacuum gripper..... 30
Figure 19. Schematic diagram of the robotic Pick-n-Place operation..... 31
Figure 20. Spatial description and representation of printing platform..... 33
Figure 21. Multi-Media Manufacturing Platform assembled overview..... 35
Figure 22. (a) A schematic graph of the DIW setup where the syringe can move in the x- and z- directions and the motion stage can move in the y-direction. A pressure regulator is used to control the pressure applied to the syringe. (b) A photo of the DIW experimental setup. (c) A microscope image of a cross section of written silver wire on the elastomer substrate. (d) A silver pattern on a TangoBlack substrate written by the DIW setup..... 38
Figure 23. The experimental setup for measuring the electro-mechanical properties of cured silver wires. A dynamic mechanical analysis (DMA) tester was used to conduct mechanical tests for the stress-strain behaviors and a multimeter was used to measure the resistance change during the mechanical tests..... 39
Figure 24. TGA (red line) and DSC (black line) measurements of the ink during curing: Heated from 40.00°C to 600.00°C at 10.00°C /min. The specimen mass: 18.343 mg for TGA, and 13.790 mg for DSC. The derivative thermogravimetry (DTG) curve is also shown in black color..... 42
Figure 25. Resistance change during curing at 80°C, 100°C, 120°C, 140°C for about 60min..... 43
Figure 26. Calculated resistivity cured at different temperature for 60min and compared with bulk silver..... 45
Figure 27. Comparison of SEM image of surface morphology: as dried, cured for 30 min at 80°C and cured for 30 min at 180°C..... 46

Figure 28. Stress-strain curves of printed silver wires and normalized resistance change when stretched, taking 80°C 20min and 140°C 20min cured samples as examples. The inserted image shows how to obtain yield strain and stress from the stress-strain curve of the 140°C 20min cured sample. 48
Figure 29. Arrhenius plot of electrical conductivity of Silver conductive wires 50
Figure 30. Conductivity variation of the silver conductive wires as a function of cure temperature and cure time. 50
Figure 31. Eg and σ_{con} values estimated for different cure times 51
Figure 32. Modulus as function of cure time and cure temperature. 52
Figure 33. Yielding (point of intersection of tangents) behavior as a function of cure time and temperature (a) yielding strain; (b) yielding stress. 53
Figure 34. Ultimate elongation (R/R0 <100 or sample crack) as a function of cure temperature and cure time. 54
Figure 35. Repeatability of printed silver wire (a) Cyclic stress-strain curves of silver wire that conducted by 25MPa/min DMA stress control (~1.3%/s) hold for 0.5min during every cycle, repeated for 100 cycles. (b) Selection of 1, 2, 5, 10, 20, 50, 100 cycles, and normalizing the initial strain of each cycle to 0. (c) Modulus of selected cycles. (d) Normalized transient resistance change as function of repeated cycles. (e) Strain shift as function of initial strain and repeated cycles. (f) Normalized transient resistance change during cyclic loaded/unloaded test as function of initial strain and repeated cycles. 59
Figure 36. Fully printed stretchable cable by embedded silver wire into PolyJet 3D printed parts: (a) The design of the cable. (b) The cross-section of the stretchable part of the cable. (c) The images of the printed part during the printing process. (d) Embedded silver wires in elastomer as circuits during stretching. Images of the printed cable under tensile strain of (Ⅰ) 0% and (II) 40% and (Ⅲ) under folding. 62
Figure 37. As printed and CAD representation of flex sensor 63
Figure 38. Calibration data for flex sensor, correlating resistance to bending angle 64
Figure 39. Images of a bending sensor on a finger-ring mounted on the forefinger, in straight (I) and bent (II and III) positions 65
Figure 40. Raw and filtered changes in bending angle measured by the embedded silver strain sensor undergoing different bending tests. 65
Figure 41. Tension Test of (a)Inkjet and (b) DIW materials 67
Figure 42. Dynamic Mechanical Analysis of Inkjet and DIW materials 68
Figure 43. CAD representation and printed parts with different geometric interfaces. 69
Figure 44. Interface strength under tension of Blunt interface geometry 70
Figure 45. Interface strength under tension of Buzzsaw interface geometry 71
Figure 46. Interface strength under tension of Lap Joint interface geometry 72
Figure 47. Comparison of interface strength of various interface geometries 73
Figure 48. Car wheel replica Hybrid 3D printed with Inkjet and DIW materials 74
Figure 49. Cross section schematic of soft pneumatic bending actuator 75
Figure 50. CAD representation and optical image of Hybrid 3D Printed pneumatic soft actuator 76
Figure 51. Pneumatic soft actuator a) deflated and b) pressurized 77
Figure 52. CAD representation and optical image of Hybrid 3D printed pneumatic soft robotic claw gripper 77
Figure 53. Schematic diagram of the shape memory cycle 78

Figure 54. Optical images of 3D printed SMP coin with channels and printed silver heating element, with thermal images during the activation of the heating element..... 79
Figure 55. Images of the printed coin progressing through the shape memory cycle 80
Figure 56. Digital LED lamp a) cross section and b) CAD rendering..... 81
Figure 57. Integrated printing process of embedded chip LED. a) FDM printed structure with pocket for LED, b) silver wires printed with chip LED placed in the pocket, c) FDM printing encapsulating the LED and silver wires, d) fully encapsulated device. 82
Figure 58. Functional printed digital LED lamp..... 82
Figure 59. Hybrid 3D Printed capacitor with (a) silver interlocking comb electrodes and (b) the final capacitor with inkjet material enclosing the electrodes 84
Figure 60. Experimental results of the capacitor used in (a) RC low pass filter circuit. (b) The input and output voltage at low frequencies shows little attenuation. (c) Frequency response of the RC filter with varied external resistance 85

LIST OF SYMBOLS AND ABBREVIATIONS

AJ	Aerosol Jetting
AM	Additive Manufacturing
CAD	Computer-Aided Design
DIW	Direct Ink Writing
DMA	Dynamic Mechanical Analysis
DSC	Differential Scanning Calorimetry
DTG	Derivative Thermogravimetry
FDM	Fused Deposition Modeling
H3D	Hybrid 3D
IC	Integrated Circuit
NPs	Nanoparticles
PCB	Printed Circuit Board
PID	Proportional Integral Derivative
PIP	Photopolymer Inkjet Printing
PWM	Pulse Width Modulation
SEM	Scanning Electron Microscopy
SLA	Stereolithography printing
SMP	Shape Memory Polymer
STL	Stereolithography file format
T_g	Glass Transition Temperature
TGA	Thermogravimetric Analysis

SUMMARY

The advent of Additive Manufacturing, also commonly referred to as 3D Printing, has enabled the rapid production of parts consisting of complex geometries that are extremely labor-intensive or even unrealizable with the use of traditional manufacturing methods. Current technologies exist that are able to print parts composed of multiple materials within a single platform, but the library of usable materials is restricted to certain subsets that are dependent on the technology being used.

In this thesis, the concept of Hybrid 3D Printing is introduced as a solution to the limited range of materials that can be printed concurrently. Hybrid 3D Printing can be described as the integration of multiple additive manufacturing process within a single platform. The design and development of a Multi-Media Manufacturing Platform is presented, detailing the technologies used and how they are integrated to enable printing of multiple materials using different additive manufacturing methods. The technologies used include Aerosol Jetting, Fused Deposition Modeling, Direct Ink Writing, Photopolymer Inkjet Printing and the non-additive processes of photonic curing and robotic pick and place.

The increased functionality of printed parts relies on the properties of the build materials used. A silver based ink is studied to provide electrical functionality within printed parts. The thermal curing effects on the electromechanical properties of a silver nanoparticle ink are investigated. From this study, thermal curing conditions are prescribed for application specific uses from stretchable electronics to sensing and heating elements. Potential applications of Hybrid 3D printing are highlighted by using the developed

platform and the silver ink, including printed/embedded electronics, soft robotics, and smart structures.

CHAPTER 1.

INTRODUCTION

The advent of Additive Manufacturing (AM) or 3D Printing has enabled the rapid production of parts consisting of complex geometries, traditionally extremely labor intensive or even impossible to realize. Recent advancements in AM have opened new and exciting avenues into applications that were previously thought to be impractical or even impossible. AM has grown from the early developments in machines that were able to print a single build material to more sophisticated machines and technologies that enable the fabrication of a single part consisting of multiple materials. The technological improvements in AM processes and methods has moved the industry from printing hobby-level/prototype parts to final production parts for consumer use. The technological improvements were driven by years of research from both the academic and industry sectors and is still a heavily researched area, with new AM technologies being discovered weekly. While lots of work has gone into individual printing technologies, many with capabilities to print multiple materials, the idea of integrating multiple AM technologies into a single platform has not been explored. AM is nearing an inflection point, as printing technologies are maturing and becoming widely adopted in many industries, where different 3D printing technologies will start to be integrated into single platforms with goals of pushing the current boundaries of AM, creating new things and exploring new possibilities[1].

The concept of Hybrid 3D (H3D) printing is introduced as the overarching theme that encompasses the integration of the different AM methods and technologies into a single platform and process. H3D printing utilizes the core strengths of individual printing technologies and combines them into a single architecture that enables more freedom in the fabrication of complex parts. By introducing the idea of H3D printing, many possible areas of research and new frontiers are opened including but not limited to; fully printed electronic devices, printing of heterogeneous materials not printable by the same technology, structures with electrical sensing capabilities. Beyond the ability for more functional parts that can be printed, new areas of design for AM and software will need to be developed for the increased capabilities and intricacies associated with integrating different processes. Another big area of interest will be the study of dissimilar materials that will be printed together and how they interact with each other. While the concept seems promising, lots of work must be done to turn it into a reality.

Researchers from UTEP have developed multiple machines and AM systems that allow for multiple material printing including a system that combines two Fused Deposition Modeling machines, enabling the printing of multiple materials with different processing parameters[2]. They have also developed a stereolithography system utilizing two resin vats to produce parts printed form two different materials again with different processing parameters[3, 4]. In addition to custom built machines, there are commercial 3D printers that can print multiple materials with different mechanical properties including the Connex series printers from Stratasys that utilize a PolyJet technology to print a library of materials ranging in mechanical properties from elastomeric to rigid plastics. Several FDM machines and academic developed research tools allow to multiple materials to be

printed together. To date, little has been done to in what might be considered true H3D printing with the exception from the previous group at UTEP and another at Imperial College of London. The group from UTEP has developed a printing system that integrates Direct Ink Writing and Stereolithography for printed structural electronics[5], while the group in London has built a system comprised of two inkjet printheads and a single direct ink writing printhead that was used to demonstrate potential capabilities of printing with three materials from different technologies[6]. While these systems and machines provide opportunities to print multiple materials, the addition of more printing technologies can further push the envelope in AM and is what is intended of this thesis.

1.1 Additive Manufacturing Methods

A brief introduction into different AM technologies will be discussed in this section to provide an understanding for the main technologies involved in throughout this thesis. Although there are many AM technologies that exist, this thesis will focus on four including Fused Deposition Modeling (FDM), Photopolymer Inkjet Printing (PIP), Aerosol Jetting (AJ) and Direct Ink Writing (DIW). These methods are chosen over others as the build material can selectively be deposited and does not require resin vats or power beds used in other AM technologies including Inkjet Binding, Selective Laser Sintering and stereolithography.

1.1.1 Fused Deposition Modelling

FDM is one of the most common 3DP technologies and was invented over 20 years ago by Scott Crump, who later founded Stratasys LLC[7]. Like all other 3D printing methods, FDM creates a three-dimensional part from a computer designed solid. FDM can

be described simply as a process where a solid thermoplastic filament is liquified and extruded out of a nozzle with applied pressure. The process involves two main components, the extruder and the hotend. The extruder is responsible for controlling the flow of the filament into the hotend, while the hotend controls the temperature of the melt chamber and nozzle, allowing for the material to be extruded. The extruder consists of a stepper motor which pinches the filament between a roller and a gear attached to the shaft. The filament is pinned between the two and any rotation of the motor results in pushing or pulling the filament into or out of the hotend. The hotend consists of an aluminium block with an internal resistive cartridge heater used to heat and melt the thermoplastic filament above an attached nozzle. The liquified filament is pushed through the nozzle by the upstream solid filament controlled with the extruder. The motion of the printhead is synchronized with the material extrusion to precisely deposit the molten thermoplastic material in a layer by layer fashion resulting in solid 3D part. A schematic representation of the FDM extrusion process is shown in Figure 1.

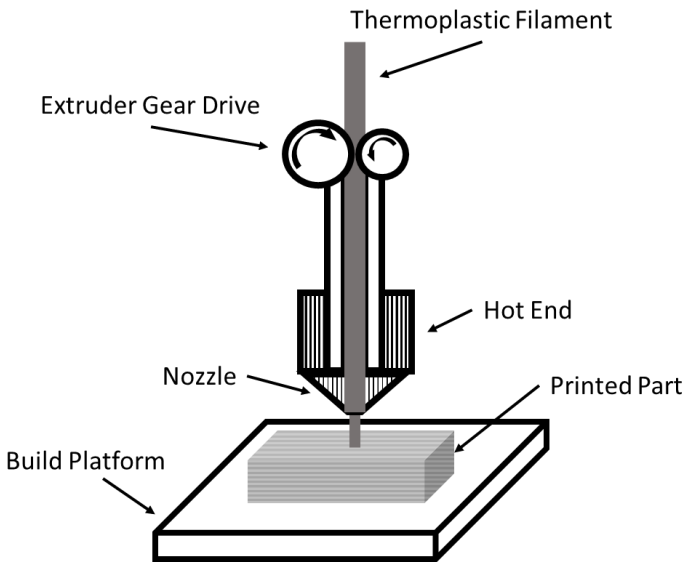

Figure 1. Simplified Schematic of Fused Deposition Modeling

1.1.2 Photopolymer Inkjet Printing

Photopolymer Inkjet Printing (PIP), works along the same principles as typical office document inkjet printers, but instead of printing ink onto paper it prints a photopolymer resin that can be cured and transformed into a solid. PIP, is another layer by layer process that utilizes an array on inkjet printheads to deposit droplets of the photopolymer onto a build plate in a defined pattern, representing a single slice of a 3D modelled solid. Each layer is jetted and wiped into a smooth film and cured with a strong ultraviolet (UV) light source. Once the layer is cured the printhead moves up allowing for material to be jetted on top of the previously cured layer and the process in repeated until a final structure is achieved. The array of printheads each have an individual build material that allows for multiple materials to be printed within the same part. A schematic representation of the printing process is shown in Figure 2.

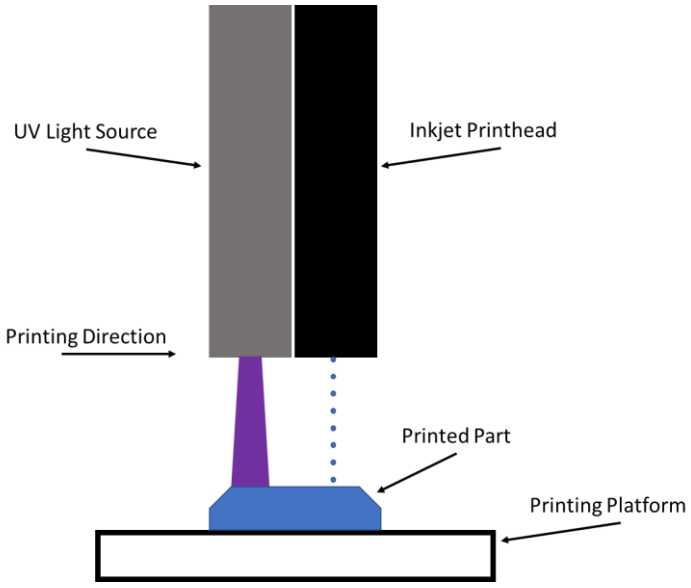

Figure 2. Photopolymer Inkjet Printing simplified schematic

1.1.3 Aerosol Jetting

Aerosol Jetting (AJ) is an additive manufacturing technology that has been developed in recent years from Optomec, the original patent holders[8, 9]. Aerosol Jetting is used in the printed electronics area for applications including antennas, interconnects and thin-film transistors [10, 11]. The AJ process starts with the atomization of a liquid material that produces droplets with diameters of a couple micrometres. The droplets are mixed with a carrier gas creating a fine mist of ink filled droplets that are transported to the print head. The mist is then condensed using a sheath gas that narrows the focus of the mist as it exits the nozzle and lands on the substrate. The material deposited on the substrate ranges in width from tens of microns to hundreds of microns allowing for high resolution printed electronics. A schematic of the AJ printing process is shown in Figure 3.

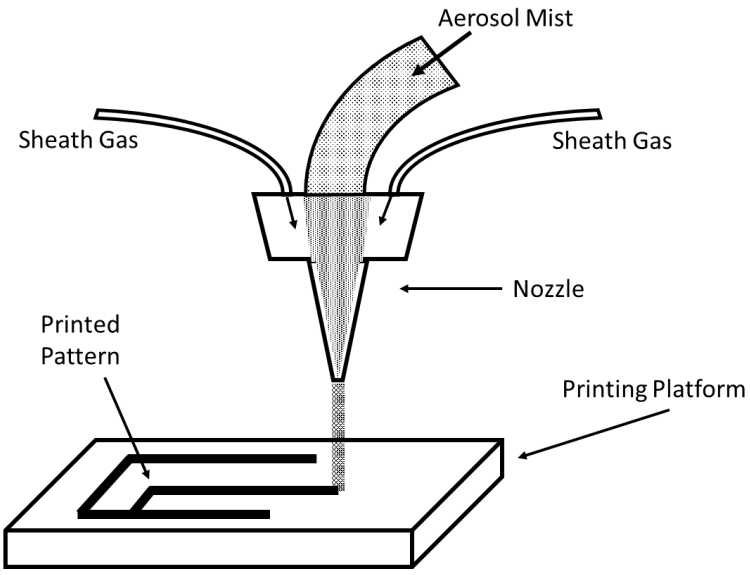

Figure 3. Simplified Schematic of Aerosol Jetting

1.1.4 Direct Ink Writing

Direct Ink Writing is an additive manufacturing process that is widely used to print pastes and gels that are suitable for other AM processes. DIW offers the unique ability to deposit materials with wide range of rheological properties, extending the library of printable materials for AM. DIW is an extrusion based technology similar to FDM as it applies pressure to a viscous material and extrudes it from a nozzle. DIW can be described as a process in which a material filled syringe is pneumatically pressurized, by means of a pressure regulator, to extrude material out of the nozzle. The nozzle size in combination with the applied pressure and rheological properties of the material determine the dimensions of the extruded line. The nozzle is moved in plane while depositing material representative of a single slice of the CAD model. After a layer has been printed, the nozzle is lifted above the previous layer and subsequent layers are printed on top of one another generating 3D solid structures. A schematic of the DIW process is shown in Figure 4.

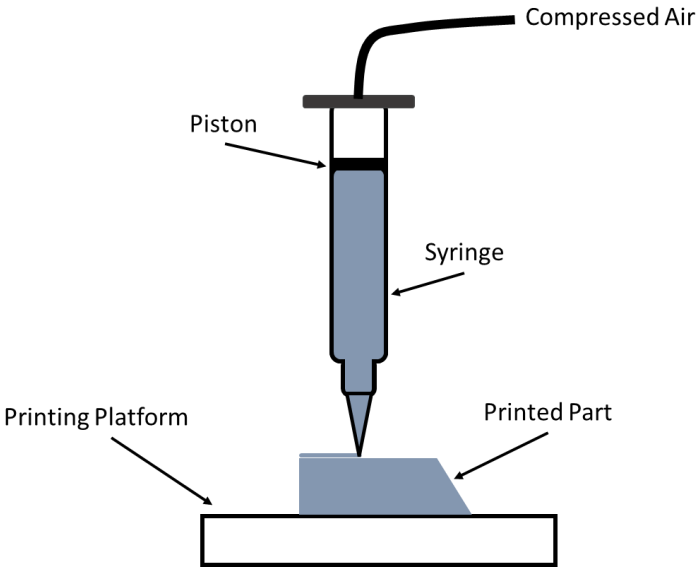

Figure 4. Simplified Schematic of Direct Ink Writing

1.2 Motivation and Objective

The three main areas of study in this thesis are the development of an integrated multi-media platform used for H3D printing, the investigation into the thermal curing effects of a silver nanoparticle ink for use in printed applications and the demonstration of capabilities and possibilities enabled with H3D printing.

The development of a new H3D printing platform involves several tasks requiring mechanical design, electromechanical system integration, control system design, circuit design, firmware and software development to name a few. The mechanical design of the platform is based on the design specifications and the overall view of the system like which AM technologies will be included, how many print heads, on what scale. The design of the platform will be introduced along with the main components being integrated. The system will be comprised of several components that must be seamlessly integrated into a single operation. Individual technologies will have to be implemented and proven before the integration of technologies can be achieved and is done so with test prints and validations. To integrate the technologies, solutions must be provided that allow for parts to go from CAD to a printed model. The main goal for this portion of the thesis is to develop a flexible platform that can be customized for specific applications and have an open framework that allows for the expansion to new technologies and processes.

With the expansion of possibilities provided by H3D printing, new materials must be developed and studied to explore potential applications and increase usefulness of printed parts. Silver nanoparticle inks are widely used in printed electronics, but the potential for stretchable conductors has not been extensively covered regarding printed

electronics and use in H3D printing. The goal of this topic is to investigate the electromechanical properties of different printed silver subject to different thermal curing conditions and develop suitable curing guidelines for use in various applications.

The potential applications for H3D printing is boundless and yet to be discovered. The final goal of this thesis is to demonstrate some potential applications in the areas of stretchable and flexible electronics, printed electronics, soft robotics, smart actuators and the printing of heterogenous materials.

1.3 Outline

This thesis is divided into five chapters. Chapter I introduces the concept of Hybrid 3D Printing and its potential applications. The current methods and applications of Additive Manufacturing are also presented and how they can be integrated to realize H3D printing. Challenges arising from H3D printing are presented and proposed solutions are presented that form the outline of this thesis.

Chapter II focuses on the design and development of an Integrated Multi-Media Platform for Hybrid 3D Printing and its associated subsystems. The mechanical and electrical design of individual modules consisting of Aerosol Jetting, Extrusion Based Technologies, Photopolymer Inkjet Printing, Photonic Curing and Robotic Pick and Place are discussed. The integration of modules is outlined and the developed software applications are presented.

Chapter III investigates the thermal curing effects on the electromechanical properties of a silver nanoparticle ink used in H3D printing. Mechanical and electrical test results are discussed and application specific thermal curing conditions are prescribed.

Chapter IV showcases various applications of Hybrid 3D Printing and examples of printed parts. Areas of applications presented include printed electronics, stretchable electronics, embedded electronics, material compatibility and soft robotics.

Chapter V summarizes the work presented in this thesis, listing the contributions made and outlines areas for potential future research.

CHAPTER 2.

INTEGRATED MULTI-MEDIA PLATFORM

This chapter describes in detail the design, development and validation of a custom built multi-media manufacturing platform. The system is comprised of AM technologies including Inkjet Photopolymerization, Direct Ink Writing, Fused Deposition Modeling and Aerosol Jetting along with a photonic curing lamp and two robotic arms for robotic pick and place applications. This system addresses many of the current limitations within 3D printing multi-material components. Challenges of printing materials with different rheological properties is overcome by incorporating multiple AM processes. The open architecture of the system provides open opportunities in many research fields of AM by giving the users full control over every parameter and process.

2.1 Layout and Design

The layout and design of the printer starts with the main requirements of the system and the subsequent design of the system. The printer should have the ability to seamlessly integrate any of the printing or processing modules into a single executable process. The ability to integrate all the printing methods should be easily implemented. For the mechanical and fundamental requirements, the printer should have a print volume of 200x200x200mm. The system should be very open leaving the possibility of future expansion and adaptation to new technologies. One major concern with designing the platform is to design a layout where all the technologies can be used fully and arrange them into the smallest form factor possible to reduce costs and practicality.

2.2 Motion System

All 3D printing systems rely on a robust motion control system to be able to precisely deposit material in desired locations. The motion system for this platform is a custom designed motion stage that was built by Aerotech Inc. (Pittsburgh, PA). The build platform, 200x200mm, for which parts are to be printed, is mounted on top of a tandem XY motion stage with 1000 and 500 mm travel distance respectively. Mounted to a granite bridge above the XY stage are 4 independent Z axes, each with 250mm of travel. Mounted on both ends of the X motion stage are Epson industrial robotic arms, a 6 axis and a 4 axis. The individual Z axis is where the printheads are mounted and each is deemed a separate "printing module". Figure 5 shows the CAD representation of the multi-media printing manufacturing platform.

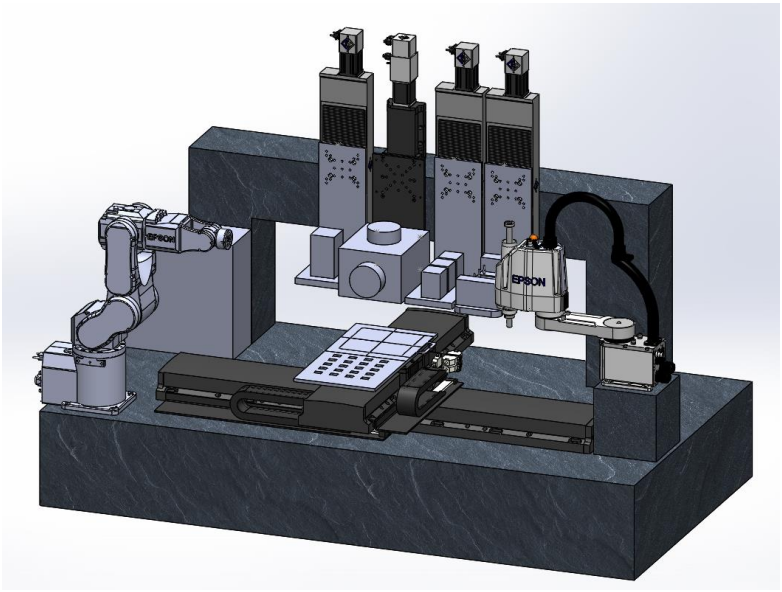

Figure 5. CAD representation of Multi-Media Hybrid 3D Printer

The main printing modules for the printer consist of the Aerosol Jetting, Photonic Curing, Extrusion, Inkjet and robotic arms modules. All motion of the system is controlled

through the Aerotech A3200 Npaq motion controller, except for the robotic arms, which have their own dedicated motion controllers. The motion for each of the stages has been calibrated and the XY planar positioning is accurate down to ±10μm and the Z axis position is accurate down to ±5μm. The X and Y axis are each equipped with an analog sine wave quadrature encoders for position and velocity feedback. The typical move profile can be described as a trapezoidal velocity profile with acceleration limiting rates and steady state velocities. The X and Y axis have upper limits of 100mm/s and 30mm/s^2. The motion controller is equipped with multiple digital and analog I/Os and some more specialized I/O functionalities that are used extensively in the printing system. The I/O functionality is used to communicate and control all the printing modules and synchronize the printing with the motion. The robotic arms are controlled with an Epson RC 700+ Motion Controller and an Epson RC 700+ Drive Unit, each having additional I/Os used to communicate with the printing modules and the Aerotech motion controller. The control architecture of the printing system is illustrated in Figure 6. The Aerotech motion controller is connected via I/O ports to the Epson RC700+ motion controller, an ATmega 2560 microcontroller and electronics of the inkjet printing module. From the I/O port of the Aerotech controller, each printing module can be controlled through a firmware developed on the microcontroller. The microcontroller is an intermediate system used to interface and control the printing modules based on inputs form the motion controllers. More detailed explanation of module architecture will be covered in the following sections.

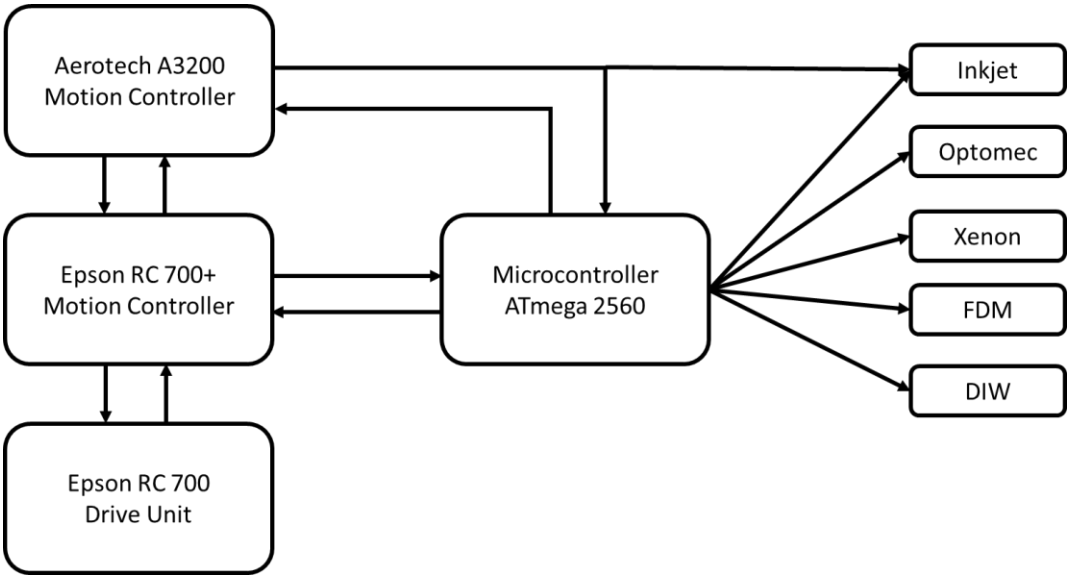

Figure 6. Operational workflow schematic of Multi-Media Hybrid 3D printer

2.3 **Optomec Print Engine**

The Aerosol Jet Print Engine is a commercial product available from Optomec Inc (Albuquerque, NM) used in advanced electronics manufacturing technologies. The print engine is used in applications including printed antennas, electronics and sensors [10-12]. The aerosol jet process creates a dense aerosol, with micron scale droplets, by atomizing a liquid sample. The aerosol mist is then transported through a virtual impactor which condenses the mist by removing excess gas and is passed along to the deposition head with an inert carrier gas. The deposition head focuses the mist into a tight beam by introducing

a sheath flow of the same inert gas to pass through a ceramic nozzle and deposit the droplets onto a substrate.

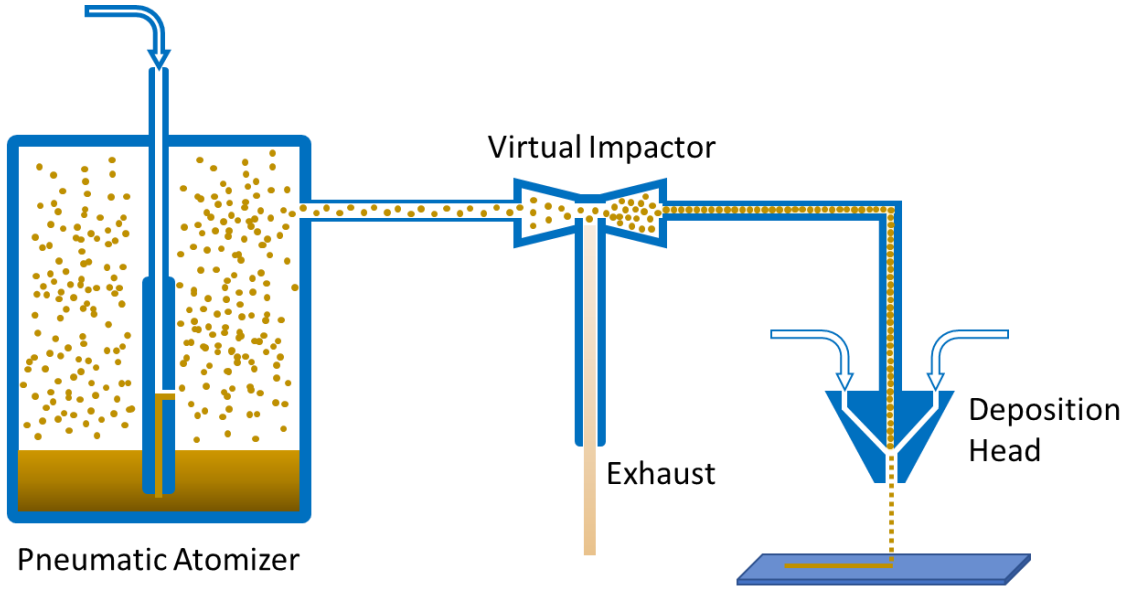

Figure 7. Schematic diagram of Aerosol Jetting based printing system

The mist is continuously passed through the nozzle while the machine is running and is only cut off by means of a mechanical shutter with a collection spoon positioned below the deposition head. A schematic diagram of the Aerosol Jetting process is shown in Figure 7. The opening and closing of the mechanical shutter is controlled by a solid-state relay connected to the shutter's motor. During printing the deposition of the aerosol mist is controlled by passing a signal from the A3200's digital output port to the ATmega2560 microcontroller which then controls the opening and closing of the relay, shown in Figure 8. The intermediate microcontroller is used to safeguard the improper dispensing of the aerosol mist as well as shift the logic levels between to two controllers.

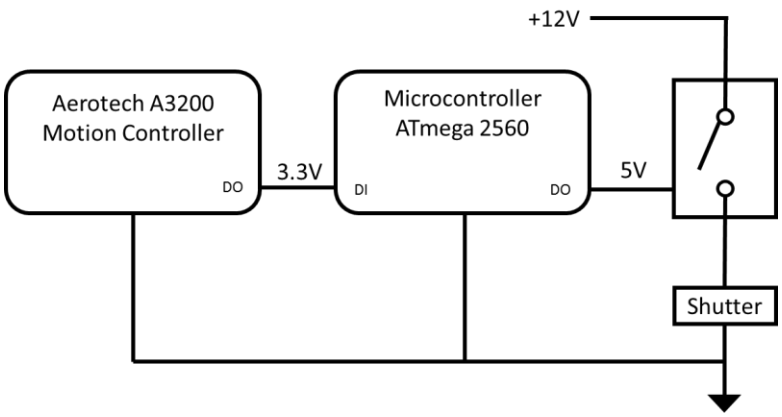

Figure 8. Schematic of Optomec Aerosol Jetting operation

The aerosol jet process is controlled by three parameters; the atomizer flow rate (Q_A), the exhaust flow rate (Q_E) and the sheath flow rate (Q_S). The parameters are chosen based on material properties and desired printing resolution. The print engine takes the user defined parameters and monitors the pressure built up within the complex pneumatic system and provides real-time feedback of the system performance.

Initial tests were performed to determine the influence of the three process parameters on the printed patterns. First, Q_A is determined by gradually increased the flow into the atomizer and monitoring the produced aerosol. Q_A is set once the atomization can be clearly seen in the form of a mist hitting the side of the material container. Next, Q_E is incrementally increasing until large drops occasionally flow through the exhaust line. Lastly, Q_S is gradually increased from zero until the desired printed line width is achieved for a set printing speed. Problems arise when Q_S becomes too large, causing the sheath flow to cut off the aerosol mist and pressure to build up within the system. Once the initial printing parameters are determined it may be necessary to fine tune the flow rates for improved printing quality. The silver nanoparticle ink for initial testing was Paru PG-007,

a silver nanoparticle ink. This ink is a versatile silver ink used quite frequently and was recommended from Optomec. Glass slides were placed on the heated printing platform and lines were printed with varying printing parameters and the results are summarized in Figure 9. The lines printed show large undesirable bulges and droplets in Figure 9a. The exhaust flow rate was increased to pull more of the big droplets out of the main supply line which feeds the head and the printed line quality was improved, shown in Figure 9b. There is still some small bulging so the parameters were fine tuned. The sheath flow was increased, removing the bulging in the printed line and printing consistent lines around 200μm in width, in Figure 9c.

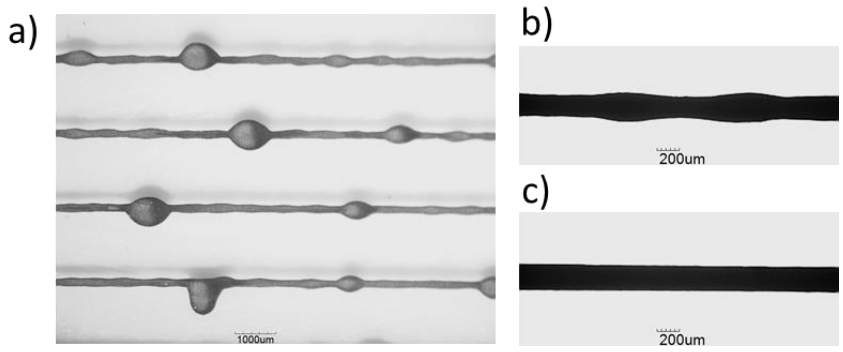

Figure 9. Microscopic Images of Aerosol Jetting printed silver lines

2.4 Xenon Photonic Curing

Photonic curing is a thermal processing technique that is becoming increasingly popular in the printed electronics industry, as it provides the ability to rapidly sinter and cure materials without damaging sensitive substrates. A photonic curing system was integrated with this platform to provide the ability to rapidly cure printed electronics without having to interrupt the 3D printing process by curing electrical circuits in an oven.

The photonic system used in this platform is the Xenon RC-847 (Xenon Corp., USA) which is equipped with a broad-spectrum flash lamp emitting wavelength ranging from 240-800nm and a 107mm diameter emitting window. This photonic system is a high frequency system able to pulse the lamp at 100Hz and delivers 19 J/pulse. The higher frequency system gives us the ability to increase the ink temperature slower than with a higher-powered system. The photonic curing system is mounted on a vertical ball screw stage above the X-Y tandem stage and lowered over the samples when curing is required. The flash lamp is controlled through the combined A3200 and ATmega microcontroller similar to the other printing modules. The A3200 uses a single digital pin to send a binary value to the microcontroller which interprets the signal and controls two solid-state relays connecting high voltage enable and trigger voltage pins on the Xenon lamp. To pulse the lamp, the high voltage enable connection must be closed allowing for the capacitors within the system to charge. After the capacitors are charged, roughly 8 seconds, the lamp then can be continuously fired by closing the trigger voltage connection. A schematic of the Xenon operation is shown in Figure 10.

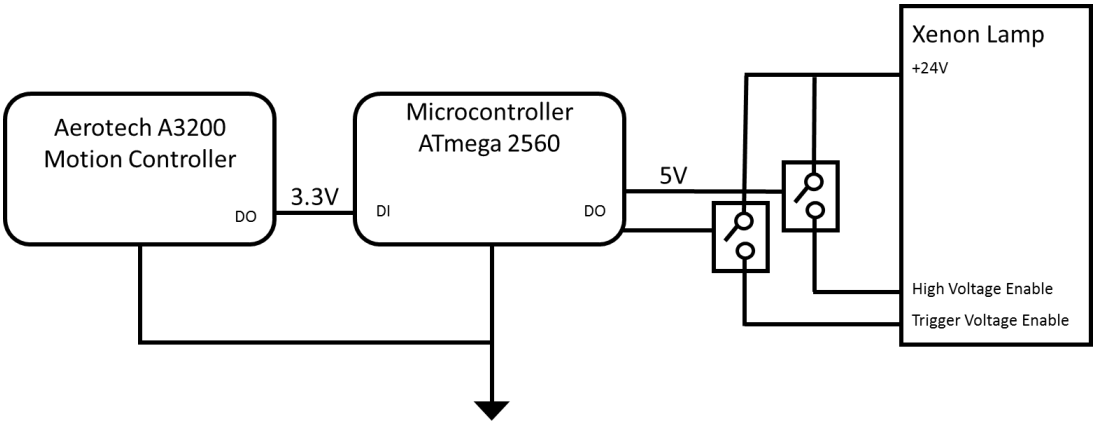

Figure 10. Schematic of Xenon Photonic Curing operation

Figure 11 shows the in-situ curing of a conductive silver nanoparticle ink. The xenon lamp is turned on, indicated by the energy curve in blue and the resistance of the silver ink is plotted during the curing. The figure is provided as a simple demonstration of the functioning Xenon lamp, showing the silver being cured as the sample is being irradiated. Further thermal curing effects of the ink will be studied in Chapter 3.

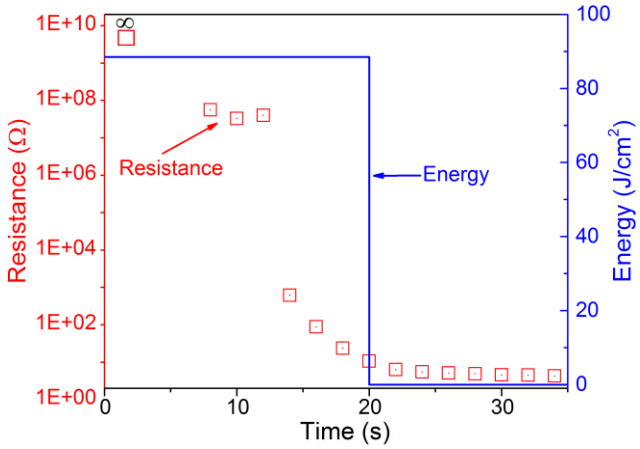

Figure 11. In-Situ resistance measurements of silver ink being cured by Xenon Photonic Curing System

2.5 Extrusion Based Technologies

Extrusion based technologies are one of the most commonly known 3D printing methods, specifically FDM, pioneered by Stratasys LTD more than 20 years ago[7]. FDM is an industry standard in printing thermoplastics and is a relatively mature and developed technology. DIW on the other hand is a newer, lesser known technology that is becoming increasingly popular because of the wide range of printable materials.

2.5.1 Fused Deposition Modelling

Two FDM printheads are used in the extrusion module. A Dyze, high temperature precision extruder and a E3D Titan extruder were chosen for the system. The Dyze is chosen for its ability to print high temperature thermoplastics such as polyether ether ketone (PEEK) and polycarbonate (PC). The Titan is a versatile extruder capable of printing common thermoplastics, ASB, PLA but also is effective at printing flexible filaments like thermoplastic elastomer (TPE) and thermoplastic polyurethane (TPU). An FDM printhead can be split into two main components, the extruder and the hotend. The extruder uses a stepper motor connected to a gearbox that turns a slotted roller, pulling the filament through the extruder and forces it into the melt zone and out the nozzle. The hot end refers to the two previously mentioned parts, the melt zone and the nozzle. After the filament passes the extruder, it enters the melt zone where the thermoplastic filament is liquified. The solid filament above the melt zone acts as a piston, pushing the liquified material out of the nozzle and solidifies shortly after exiting the nozzle tip. The extrusion process is controlled by the rate at which the filament is forced through the extruder resulting in the volumetric flow rate Q_e [13, 14],

$$Q_e = \pi r_f^2 R\omega$$

where r_f is the filament radius, R is the slotted roller radius and ω is the angular velocity of the slotted roller. The volumetric flow rate out of the nozzle, Q_n is:

$$Q_n = \pi r_n^2 v_n$$

Where r_n is the nozzle radius and v_n is the exit velocity of the liquified material. By equating the flow rates, we can derive the angular velocity of the slotted roller given a desired material exit velocity:

$$\omega = \frac{r_n^2 \, v_n}{r_f^2 \, R}$$

With the required angular velocity to deposit material from the nozzle with the same flow rate as the input to the melt zone the stepper motor can be controlled to step at a specific frequency to produce a specific exit velocity. The X-Y motion stage is set to a certain printing speed, v_p, for all planar movements during printing. By matching the printing velocity and the exit velocity filaments with consistent geometries can be deposited. A scaling factor, α, can be introduced to over/under fill material during printing resulting in the control of the deposited line width and height.

$$v_n = \alpha v_p$$

The stepper motor can be controlled based on the set printing speed and scaling factor. During printing a square wave with a set frequency, f_s, can be used to step the motor during print moves, where β is the steps per revolution of the stepper motor:

$$f_s = \frac{\beta \mu_s r_n^2 \alpha v_p}{2\pi R r_f^2}$$

The Pulsed Synchronized Output (PSO) from the A3200 controller is a specialized output that is used to generate a pulse train between 0 and 3.3V into the stepper driver step pin. The PSO is configured in the A3200 software and is set to the stepper frequency with

a 50% duty cycle. The stepper driver must also be enabled and have a defined direction, which are controlled through the A3200 and ATmega microcontroller digital outputs as well. The schematic illustration of the FDM printhead operation is shown in Figure 12.

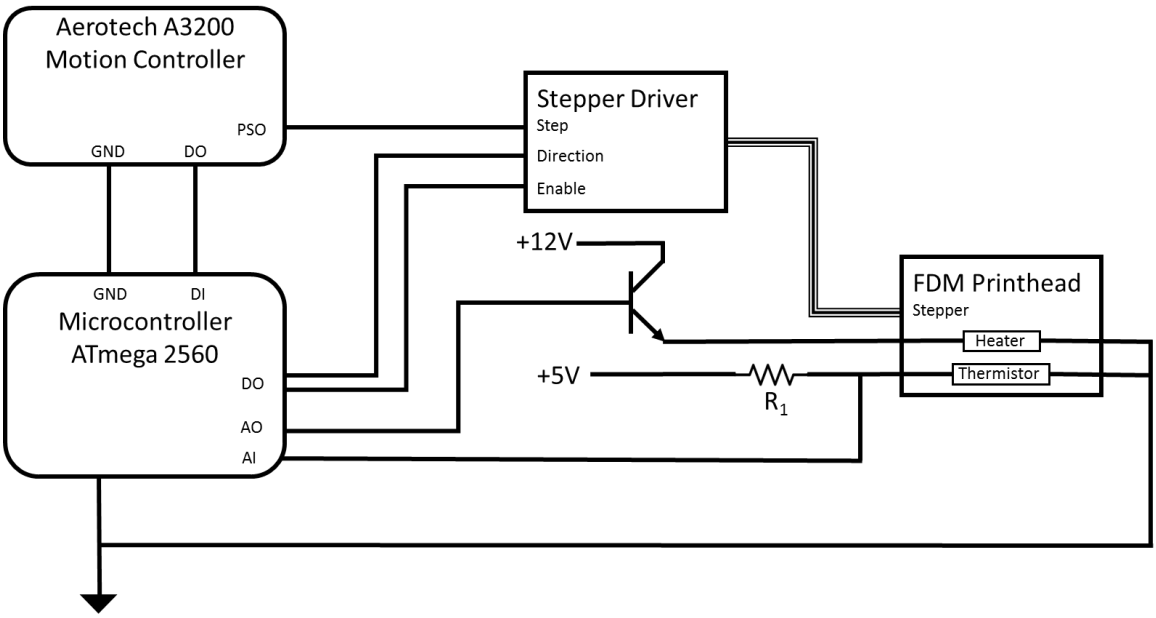

Figure 12. Schematic of FDM printhead operation

The temperature control of the printheads is controlled through a combination of a resistive cartridge heater and a thermistor used in a feedback control system. A PID controller was designed to control the temperature of the hotend and implemented in the ATmega microcontroller. The heater is controlled with a pulse width modulated (PWM) signal able to vary the average applied voltage to the heater between 0 and 12V. A 10kΩ thermistor was used to measure the temperature of the hotend by building a voltage divider connected to an analog input of the ATmega microcontroller. The PID controller calculates

the error, e, as the difference in measured temperature, $T_{m,}$ and the temperature setpoint, T_s. The input, u, to the heater is a PWM value saturated between 0 and 100.

$$u(t) = K_p e(t) + K_i \int_{-\infty}^{t} e(t)dt + K_d \frac{d}{dt} e(t)$$

The printhead hotend can be modeled using Fourier's Law and the heat equation, resulting in the governing dynamic equation:

$$(R_T C)\dot{\tilde{T}} + \tilde{T} = R_T Q_{in}\ , where\ Q_{in} = \frac{V_H^2}{R} = \frac{(V * DC)^2}{R}\ and\ \tilde{T} = T_H - T_\infty$$

where R_T is the thermal resistance of the hotend walls, C is the thermal capacitance of the hotend, T_H is the temperature of the hotend and T_∞ is the ambient temperature, V_H is the voltage drop across the heater, Q_{in} is the applied heat to the hotend and V as the common voltage supply. Taking the Laplace transform yields the following transfer function for the hotend:

$$(R_T C)sT(s) + T(s) = R_T Q_{in}(s) \rightarrow \frac{T(s)}{Q_{in}(s)} = \frac{R_T}{(R_T C)\ s + 1}$$

The hotend can be modeled as a first order system of the form:

$$G(s) = \frac{T(s)}{D(s)} = \frac{K}{\tau\ s + 1}$$

Where K is the control effectiveness and τ is the time constant of the system. The response of the heater controlled with the developed PID controller can be seen in Figure 13.

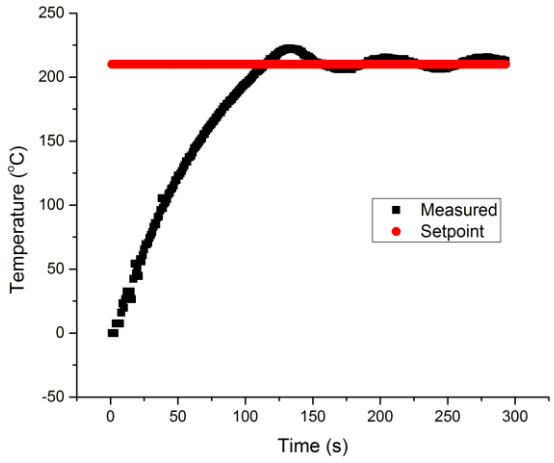

Figure 13. Temperature response of hotend under PID control

2.5.2 Direct Ink Writing

The DIW portion of the extrusion module is based on the Nordson EFD UltimusV precision dispenser. The dispenser can precisely control the pressure applied to a fluid filled syringe. The UltimusV has a single output port, which can limit the ability to print multiple materials with the single unit. To overcome the single material constraint, an external switching device was developed which can split the output flow between two individually controlled syringes and can be expanded to an arbitrary number of syringes to provide advanced multi-material printing capabilities. The UltimusV is another printing module that is controlled through the digital output of the Aerotech Motion controller. The Aerotech motion controller sends a high/low bit to the microcontroller, which then sends a signal to the UltimusV that initiates a dispensing cycle. The UltimusV continues dispensing

the fluid until another signal is sent to the microcontroller from the Aerotech motion controller. While dispensing, the motion of the syringe nozzle is controlled allowing for the formation of complex 3D objects. A simplified schematic outlining the operation of the DIW is show in Figure 14.

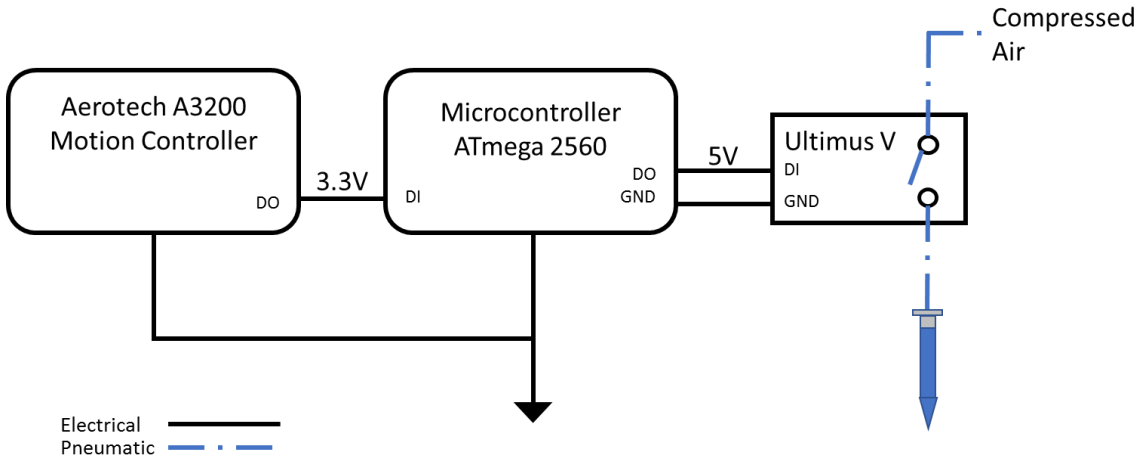

Figure 14. Schematic of DIW operation

2.6 **Photopolymer Inkjet Printing**

Photopolymer inkjet printing is one of the more difficult AM technologies. The material requirements are one of the main restricting factors of inkjet printing. The rheological properties of the materials to be used are very specific and limiting. Specific requirements on the materials viscosity and surface tension are defined for particular printheads and puts tight constraints on the materials available to use.

The photopolymer inkjet printing module consists of, 4 Xaar 1003 (Xaar Plc, England) piezoelectric drop on demand printheads, two Phoseon FE300 UV LED lamps, a Xaar Hydra ink supply system and Xaar control electronics. The 1003 model offers a relatively large range of printable viscosities, 8-25cPs. The printheads have a native resolution of 360 dpi and a 70.5mm print swathe. The printheads are fed with a Xaar Hydra ink supply system capable of precise meniscus pressure control and fluid temperature control. The UV lamps provide an adjustable light intensity of up to 5W/cm^2. The ink used in the development and testing of the printhead is ETIJET ULX5832 (SunJet, DIC Inkjet Solutions). The inkjet printheads are capable of printing in 360 dpi in line with the printhead axis and have no firm limit on the resolution in the scanning direction. Grayscale images are loaded to the printhead via the XUSB Driver, the electronics interface between the printheads and the computer. Once the image is loaded to the controller two signals are needed to properly print, the encoder input and the product detect input. The product detect input is a digital signal used to let the printer know when the image is ready to be printed and is triggered once the motion stage is in motion and at a constant velocity. The encoder input is used as position feedback to let the printhead know when to deposit material. The encoder input is provided by the A3200 motion controller's PSO output, also used in the FDM module. The PSO output is used to fire a pulse train at a set frequency. The XUSB driver interprets the encoder signal, keeps track of pulses and fires the next row of pixels in the image depending on the frequency and a frequency divider values used for printing. The desired resolution, R_J and printing speed v_J are needed to determine the PSO jetting frequency f_J and is calculated as:

$$f_J = R_J v_J \gamma$$

where γ is the internal encoder divider value, used for high resolution encoders.

The UV lamps need two signals to operate, an enable and intensity control. The enable control is controlled by the microcontroller that switches a relay open and closed, enabling and disabling the lamp. The light intensity is controlled with an analog signal from 0-10V, corresponding to 0-100% output intensity. The schematic overview of the photopolymer inkjet printing module is shown in Figure 15.

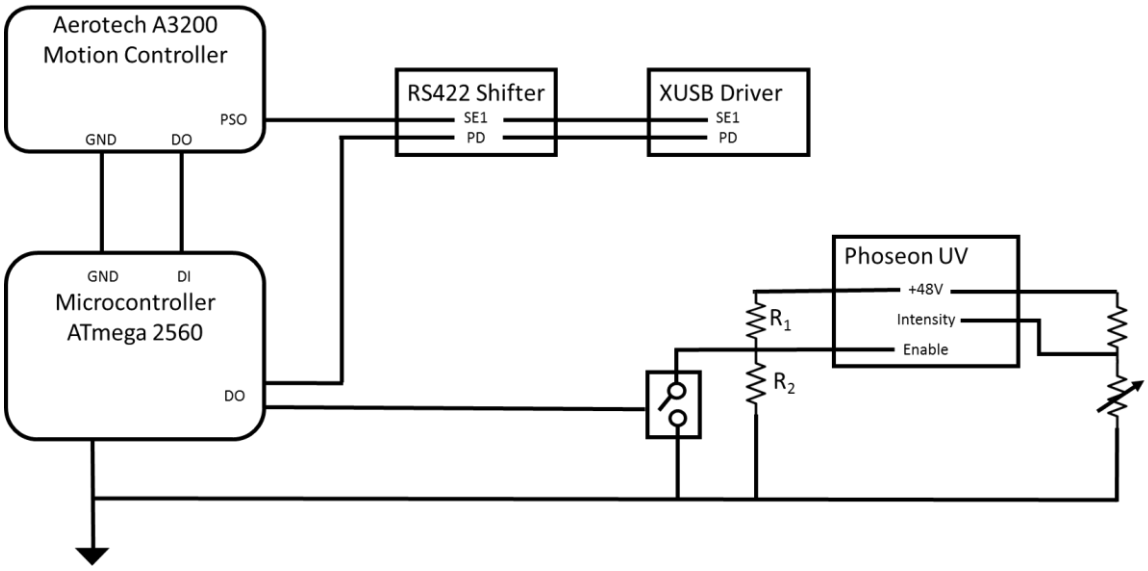

Figure 15. Schematic Diagram of Photopolymer Inkjet Printing operation

The layer thickness of the printed material can be controlled with the printing direction resolution. The higher the resolution/jetting frequency the thicker the printed layers get as a result of more material being laid down over the same image area. The effect

of changes in printing resolution have on the layer thickness are presented in Figure 16. Based on the results, the layer thickness can be set anywhere between 5 and 35μm.

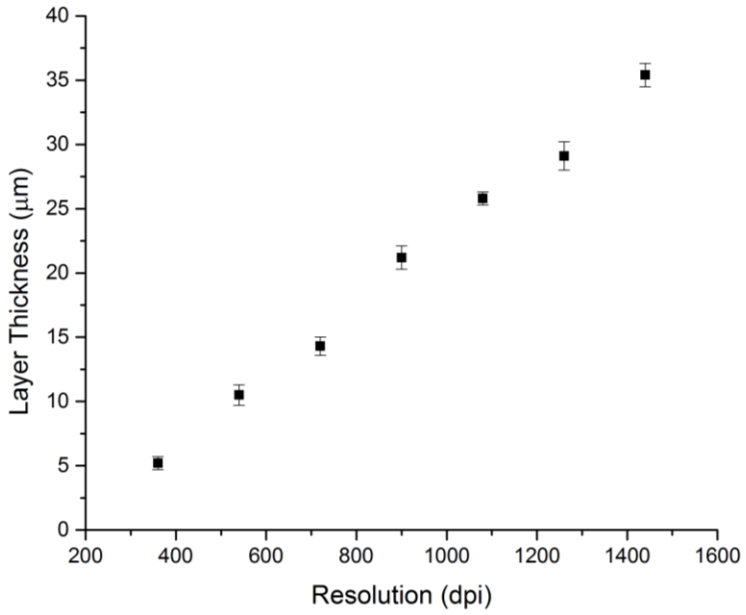

Figure 16. Layer thickness as a function of inkjet resolution

Grayscale images used in the inkjet module are generated from a commercial slicing software, Creation Workshop. STL files are loaded into the software which can orient the part and define the slicing settings, layer thickness, printing platform dimensions and image resolution. Once images are sliced, they are converted in a MATLAB script from a binary bitmap to a grayscale image and reformatted to a printable size for the inkjet module. The grayscale image is a unique feature that enables the ability to selectively vary the infill density within a single layer by changing the droplet volume based on the particular grey level. Sample parts were printed to validate the photopolymer inkjet printing module and are shown alongside their respective CAD models in Figure 17.

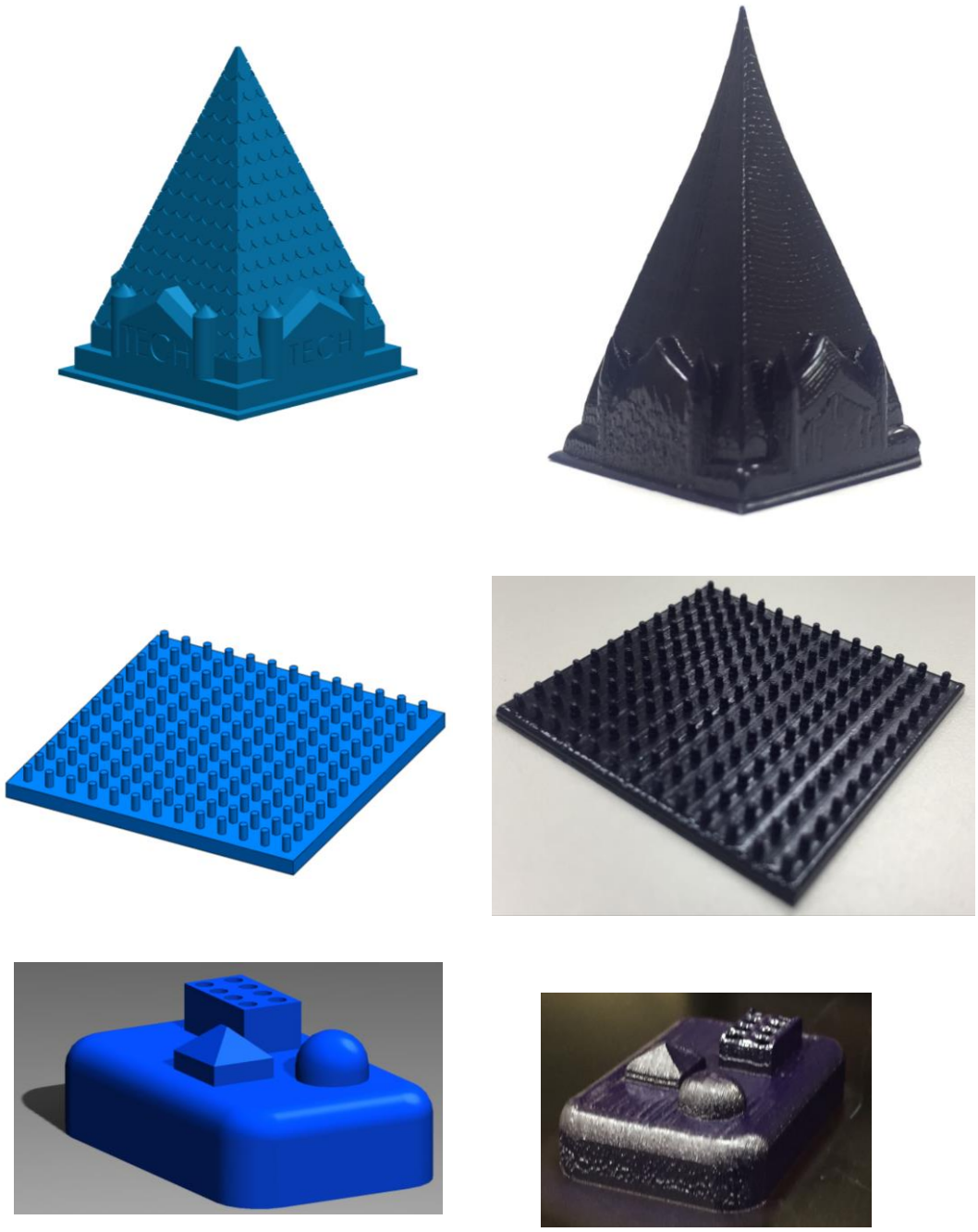

Figure 17. CAD designs and corresponding inkjet printed parts

2.7 Robotic Pick and Place

The Pick and Place module consists of two robotic arms, an Epson C6 and an Epson G4 robotic manipulators. The C6 arm is a 6-axis articulated manipulator and the G4 is a 4-axis cartesian arm. Both arms can be used for pick and place applications of non-printable components, such as ridged electronics (sensors, circuit elements and actuators), active materials or any arbitrary component. The robotic arms are controlled by an Epson RC700+ motion controller and drive unit. Both arms can be programed individually for specific applications. A pneumatic vacuum gripper was built for pick and place applications and is shown in Figure 18. The vacuum gripper consists of a vacuum pump connected to a spring-loaded suction connection for interchangeable nozzles.

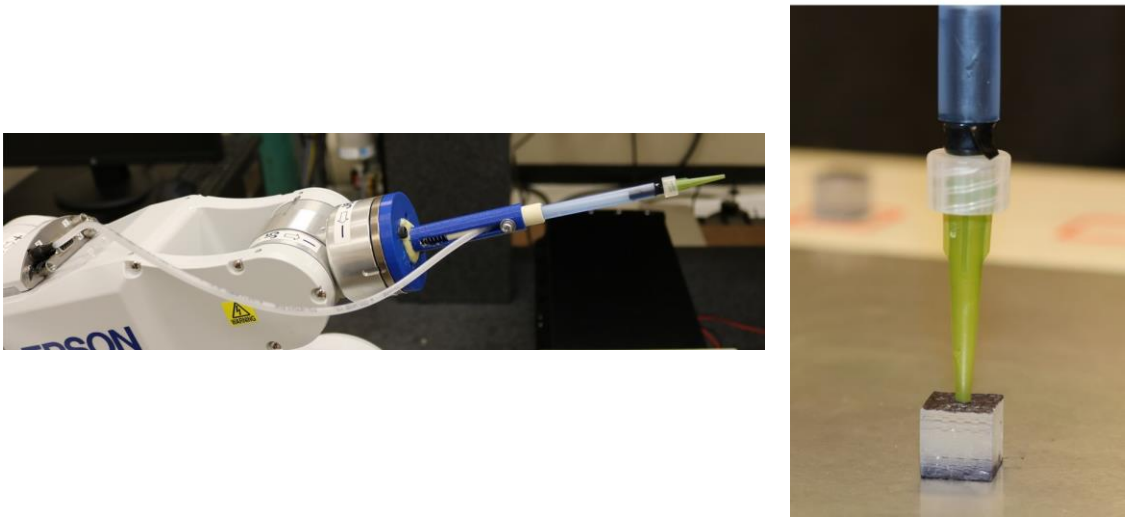

Figure 18. Robotic arm Pick and Place vacuum gripper

The nozzle size is determined based on the components being picked up, increasing in nozzle diameter with an increase in component weight as the force needed to lift heavier

objects is increased. The vacuum pump is powered by a 12V supply connected in line with a solid-state relay which can be controlled from the ATmega microcontroller and the A3200 motion controller, shown schematically in Figure 19.

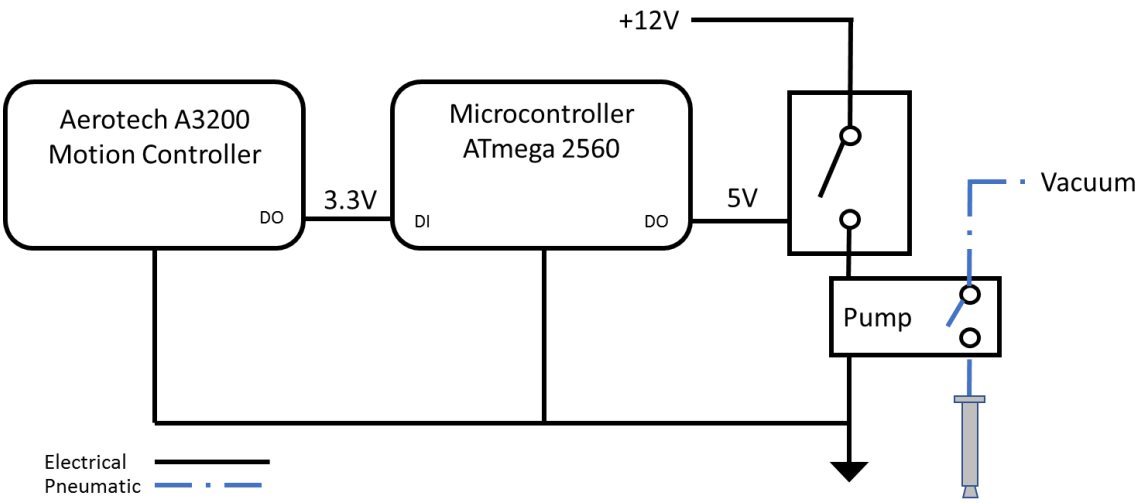

Figure 19. Schematic diagram of the robotic Pick-n-Place operation

2.8 Software and Firmware

For 3D printing, there are a lot of software packages that are specialized to a particular technology such as FDM, SLA or inkjet. For this printer, there is no integrated software that is specialized and integrated, so a method for controlling the printer was developed. The printer is controlled from a single desktop computer. Both Aerotech and Epson provide a software for controlling and programing the motion of their respective systems. The Aerotech software is used to control X, Y and all Z axis as well as many of the printing modules via the output ports previously described. The Epson software is responsible for all the motion for the robotic arms and the pneumatic vacuum gripper

control. The printer also uses multiple commercial and custom software applications during the setup and printing. First, CAD files of the models desired to print are needed, as is the same with all 3D printing. From the CAD files, there are a multiple paths the setup can take depend on the printing modules being used. For parts using the extrusion module and the Aerosol Jetting module traditional slicing software is used, in this case Slic3r was used to generate G-code toolpaths from the CAD file. For the robotic pick and place of the components parts are also imported to the assembly in Slic3r to be sliced and later post processed. For inkjet components CreationWorkshop is used to generate bitmap cross-sectional images of the STL file. G-code files are then post processed with a custom VisualBasic application to parse the G-code and change the G-code into an executable file for the Aerotech software and the Epson software. The images generated with CreationWorkshop are post-processed with a MATLAB script that changes the image format and size to work with the inkjet hardware.

Connecting the controllers via hardware (I/O ports) effectively controls the printing process while running multiple software applications simultaneously by reacting to hardware communications between them. After the printing is initiated, the I/Os of the controllers are used to communicate with each other and control all the printing processes.

2.9 Printing Methods

The integration of multiple printing technologies requires the development of different approaches to printing parts. Extrusion based and single nozzle printing applications typically rely on G-code, a point to point printing scheme, whose toolpath is generated from cross sectional slices of a solid model. Inkjet printing is one application

that can print a single layer in a few discrete movements, dependent of the object size, by utilizing the array of nozzles used to deposit build material. Bitmap or grayscale images are typically used to represent a single layer of the designed part and printed accordingly. Printing with multiple printheads creates difficulties in transitioning between printheads while maintaining accurate positioning. To reliably switch between different printheads and keep accurate positioning, kinematic transformations must be developed and applied to the generated printing coordinates, shown in Figure 20. The generated printing GCode

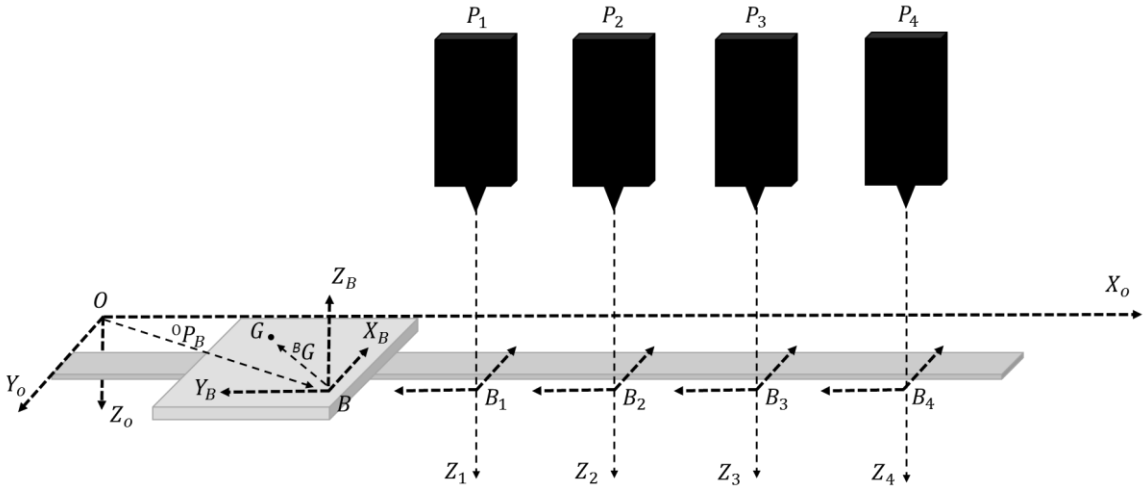

Figure 20. Spatial description and representation of printing platform

provides a toolpath in a local coordinate frame, B, on the printing platform. These coordinates cannot be directly used as all the motion is controlled through the Aerotech motion controller and its respective axis. For the G-code coordinates to be used to print between different printheads, P_i, homogeneous transformation matrices must be derived which can represent the G-code with respect to the printhead being used. First a rotation matrix is defined to represent the rotation of a general frame, B, with respect to the origin frame, O, of the XY motion stage, which consists of a 180° rotation about $X_O$and a 90° rotation about Z_O:

$$ {}^{O}_{B}R = R_{Z_O}(90)R_{Y_O}(0)R_{X_O}(180) = \begin{bmatrix} 0 & 1 & 0 \\ 1 & 0 & 0 \\ 0 & 0 & -1 \end{bmatrix} $$

After rotation, the general frame B only differs from frame O by a single translation which is dependent on the printhead being used, i, and the offsets associated with the particular printhead, $X_i, Y_i \; and \; Z_i,$ that place the origin of frame B at the point of the printhead.

$$ {}^{O}P_{B_i} = \begin{bmatrix} X_i \\ Y_i \\ Z_i \end{bmatrix} $$

Any coordinate in the G-code can be described in terms of frame B with a simple vector, ${}^{B}G$, from the origin of B.

$$ {}^{B}G = \begin{bmatrix} X \\ Y \\ Z \end{bmatrix} $$

where X, Y and Z are the coordinates from the G-code. Finally, by combining the rotation and translation matrices, any generated point in G-code, G, can now be represented in the Aerotech motion coordinates for the respective printhead, i, as ${}^{O}G^{i}$ and defined as:

$$ \begin{bmatrix} {}^{O}G^{i} \\ 1 \end{bmatrix} = \begin{bmatrix} {}^{O}_{B}R & & & {}^{O}P_{B_i} \\ 0 & 0 & 0 & 1 \end{bmatrix} \begin{bmatrix} {}^{B}G \\ 1 \end{bmatrix} $$

2.10 **Summary**

In this chapter, the design and development of the multi-media manufacturing platform has been introduced. The platform consists of AM technologies including Inkjet

Photopolymerization, Direct Ink Writing, Fused Deposition Modeling and Aerosol Jetting along with a photonic curing lamp and two robotic arms for robotic pick and place applications. Each printing module has been developed and is fully functional providing a first of its kind platform for H3D printing. The open architecture of the platform fosters the creation of various parts using different AM technologies. The platform in its current state is shown in Figure 21.

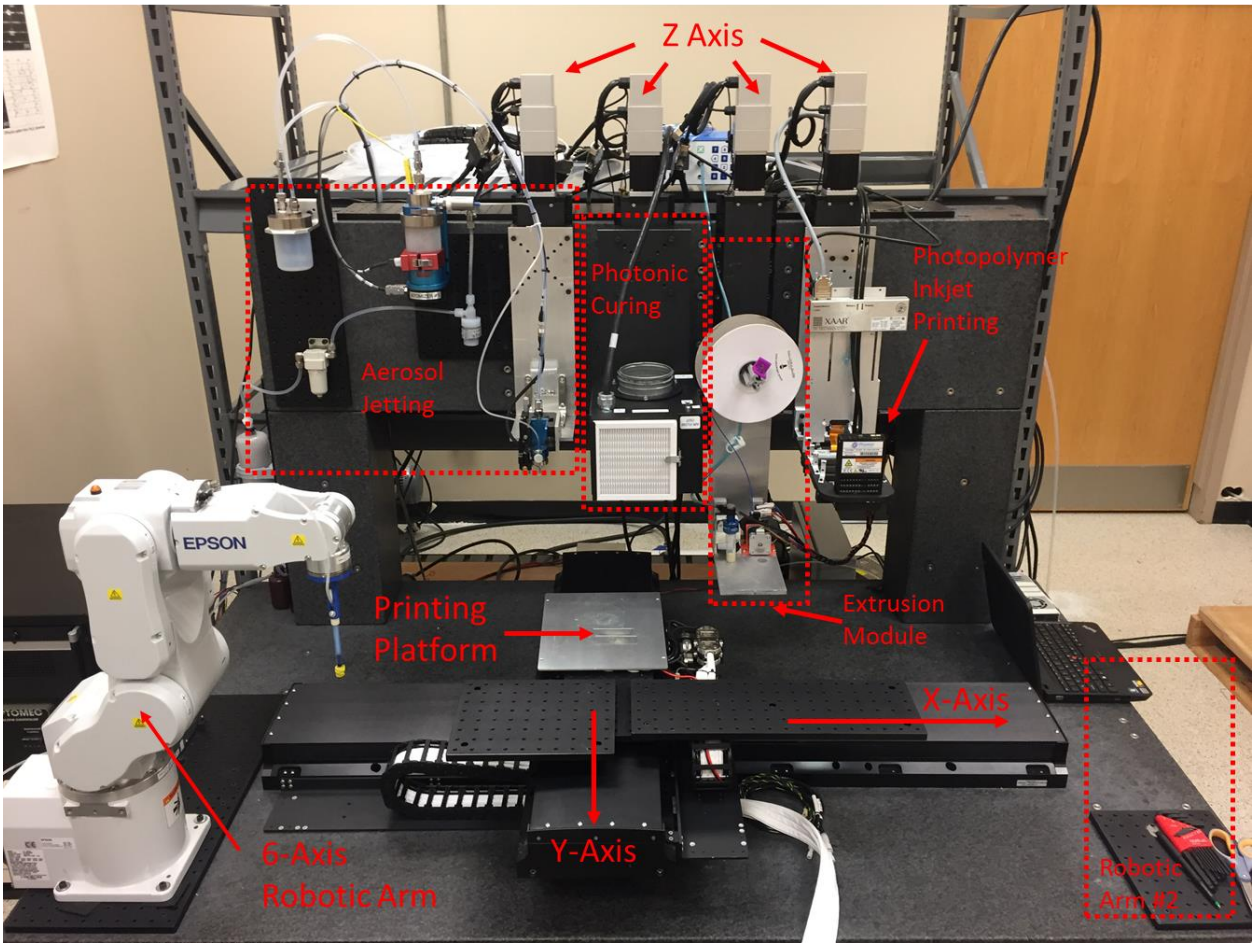

Figure 21. Multi-Media Manufacturing Platform assembled overview

CHAPTER 3.

THERMAL CURE EFFECTS OF SILVER NANOPARTICLE INK

In this chapter, the electromechanical properties of conductive wires made from a silver nanoparticle ink, printed via direct ink writing (DIW), cured under different thermal conditions and subject to various mechanical loadings are studied. The goal is to develop an understanding of the electromechanical properties of the printed wires and develop prescriptions for curing the ink to be used in various applications. Here, a commercially available silver ink, DuPont ME603 (DuPont Inc., Wilmington, DE, USA), is used. It should be noted that DuPont ME603 ink is not specifically designed for stretchable applications, but this chapter demonstrates that by properly controlling the curing conditions, the ink can be used for stretchable devices. This chapter is arranged as follows. First the materials and methods are introduced; then the effects of curing temperature and curing time by using thermogravimetric analysis (TGA), differential scanning calorimetry (DSC) measurements, scanning electron microscopy (SEM) images and in situ resistance change measurements are investigated. Further studies into the effects of thermal cure conditions on the electro-mechanical properties of the printed silver wire are presented, and the optimized cure conditions for various applications, including stretchable electronics and sensing elements are defined. The work presented in this chapter is based on a 2017 publication in *Smart Materials and Structures* [15].

3.1 Materials and Methods

3.1.1 Materials

The silver nanoparticle ink used in this study was DuPont ME603, which has a solids content of 49%-53%, viscosity of 15-35 Pa.·s and sheet resistivity <200mΩ/sq/mil. The manufacturer recommends the curing condition of 120°C -140°C in a static box oven for 10min. In this work, the ink is DIW printed onto a 3D printed elastomer substrate, namely TangoBlack, one of the model materials available in the material library of the PolyJet 3D printer Objet Connex 260 (Stratasys Inc., Edina, MN, USA). The reason for choosing a 3D printed substrate is that this work is intended to combine 3D printed materials with DIW of functional inks, and TangoBlack is a material used in our previous work on 4D printing[16-21] . In addition, it's been noticed that when the silver ink was printed onto a soft substrate such as an elastomer, it could be easily peeled off for mechanical testing.

3.1.2 DIW Setup

The silver ink was printed onto a 3D printed elastomer substrate using a DIW experimental setup, which is shown in Figure 22a. The printing platform moves the substrate along the y-direction, while a pressure controlled syringe moves in the x- and z- directions. The pressure in the syringe is controlled by a pressure regulator (UltimusV, Nordson EFD, East Providence, RI, USA). The syringe was attached to a nozzle with 0.61mm inner diameter. With a pressure of 15psi and a printing speed of 3mm/s, the silver ink was able to be printed with consistent cross-sectional areas.

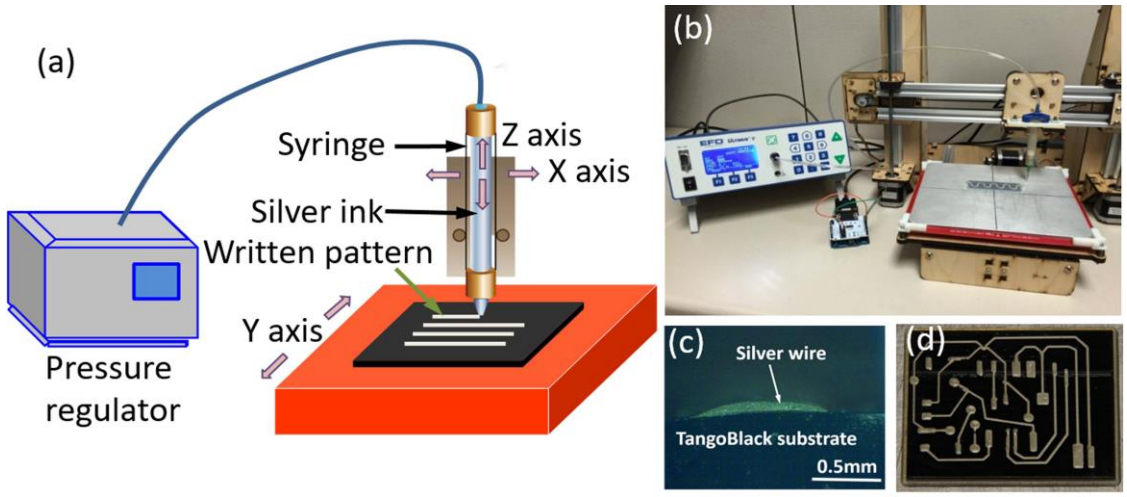

Figure 22. (a) A schematic graph of the DIW setup where the syringe can move in the x- and z- directions and the motion stage can move in the y-direction. A pressure regulator is used to control the pressure applied to the syringe. (b) A photo of the DIW experimental setup. (c) A microscope image of a cross section of written silver wire on the elastomer substrate. (d) A silver pattern on a TangoBlack substrate written by the DIW setup.

3.1.3 Thermal Curing

Once the silver ink was printed, it was cured in a convection oven (Model 13-247-750G, Fisher Scientific, Pittsburgh, PA, USA) at different temperatures and curing times. To record the resistance, change during curing, two copper electrodes were fabricated that connected the printed lines to a multimeter (Keithley2100, Keithley Instruments, Cleveland, OH, USA), which was controlled by a LabVIEW data acquisition program and sampled at 0.5-5Hz.

3.1.4 Measurement of Cross Sectional Area

To calculate the resistivity and modulus of printed silver wires cured under different conditions, the cross-sectional area of these wires should be known. Cross-sectional images

of the cured silver wires were taken with a trinocular microscope (Model 89404-886, VWR, Suwanee, GA, USA). Figure 22c shows a typical cross-section of the cured ink. The cross-sectional area was then calculated by using the open source image processing software ImageJ.

3.1.5 Stress-Strain and Cyclic Testing

After curing and measuring the cross-sectional area, the silver wires were carefully peeled off from the substrates using a pair of tweezers. The electrical and mechanical properties were then studied. A dynamic mechanical analysis (DMA) tester (Model Q800, TA Instruments, New Castle, DE, USA) was used alongside a multimeter to measure the electro-mechanical properties of cured freestanding wires. Figure 23 shows the experimental setup.

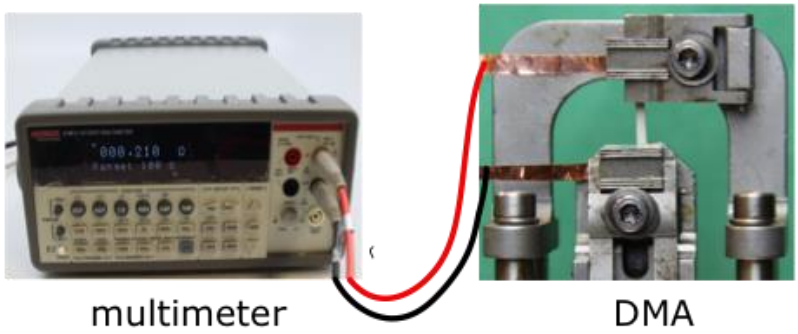

Figure 23. The experimental setup for measuring the electro-mechanical properties of cured silver wires. A dynamic mechanical analysis (DMA) tester was used to conduct mechanical tests for the stress-strain behaviors and a multimeter was used to measure the resistance change during the mechanical tests.

For the stress-strain tests, the strain control mode was used with a strain rate of 10% /min. For the cyclic loading/unloading tests, the stress control mode was used with a

stretch/release rate of 25MPa/min (corresponding to a strain rate of 0.5%/s -2%/s), and a holding time of 0.5min between cycles. The resistance change during cyclic testing was also recorded. All electromechanical property tests were performed at room temperature (22°C).

3.1.6 Resistivity

For all resistance measurements, a two-point probe method was used to calculate the bulk resistivity and its change throughout curing. Resistivity ρ was calculated as:

$$\rho = \frac{R \cdot A}{l}$$

where R is the measured resistance, l is the distance between terminals, and A is the cross-sectional area of the cured silver wire.

3.1.7 Other Characterization Methods

The microstructures of the printed wires were investigated by using a scanning electron microscope (SEM, Model LEO 1530, ZEISS, Oberkochen, Germany). The images were taken with an accelerating voltage of 10 kV. In order to identify the solvent removal and decomposition behavior of the organic additive, thermogravimetric analysis (TGA, model STA 6000, PerkinElmer, Waltham, Massachusetts, USA) was conducted between 40 °C and 600 °C at a heating rate of 10 °C min^{-1}. DSC tests were also conducted between 40 °C and 600 °C at a heating rate of 10 °C min^{-1} by using a DSC tester (Model 2000, TA Instruments, New Castle, DE, USA) to obtain the phase transition of the ink during curing.

3.2 **Effect of Thermal Curing Conditions**

3.2.1 Mass Loss During Curing

In order to choose proper curing temperatures, both TGA and DSC tests were conducted to study the mass change during curing. The TGA and DSC curves are shown in Figure 24. It can be seen that the mass of the sample decreases as the temperature increases, settling at ~54% of the initial mass. This value confirms the removal of solvents and additives and agrees with the solid content (49%–53%) of the ink according to the manufacturer. The mass reduction can be divided into three stages, which are shown by the slope change in the TGA curve and can be identified from the three peaks in the derivative thermogravimetry (DTG) curve. In the first stage, the sample's mass quickly drops 26% between 47 °C and 177 °C, with an endothermic reaction observed from the DSC curve, which may be caused by the evaporation of solvents. In the second stage, the mass sharply drops another 11% near ~200 °C, where the peak on the DSC test indicates decomposition of organic additives or removal of residual solvents. Finally, in the third stage, at around 440 °C there is another mass drop, which may be caused by decomposition of other organic/inorganic additives.

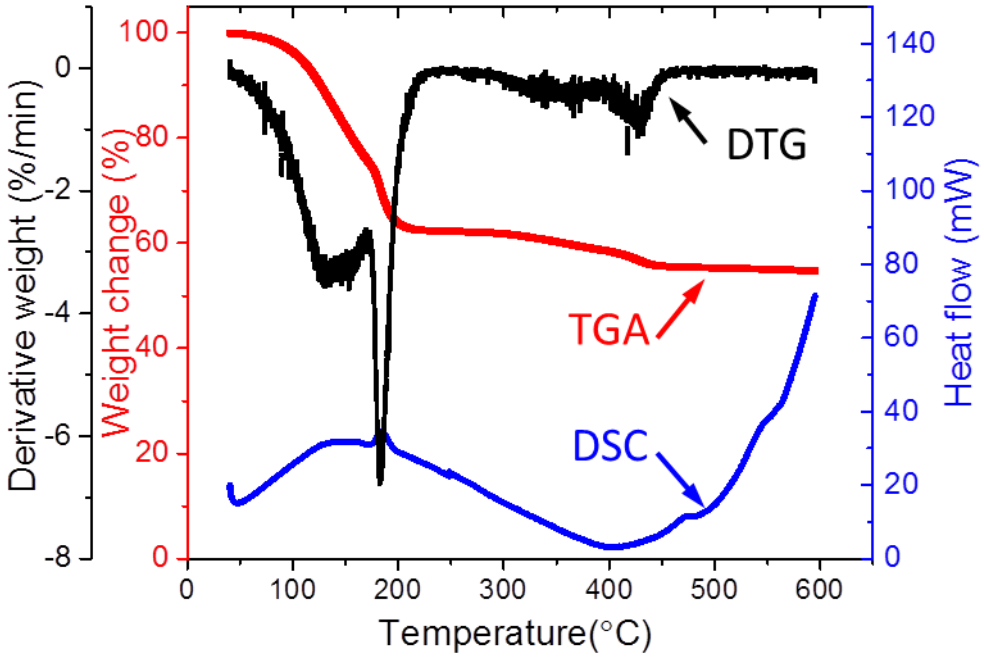

Figure 24. TGA (red line) and DSC (black line) measurements of the ink during curing: Heated from 40.00°C to 600.00°C at 10.00°C /min. The specimen mass: 18.343 mg for TGA, and 13.790 mg for DSC. The derivative thermogravimetry (DTG) curve is also shown in black color.

3.2.2 In Situ Resistance Change During Curing

The TGA/ DSC curves show that as the temperature increases, the solvent in the ink evaporates at different temperatures. Thus, the ink was cured at different temperatures in the range of 80 °C–180 °C for a relatively long time (60 min) to detect resistance changes. The curing processes at four different temperatures: 80 °C, 100 °C, 120 °C, and 140 °C are compared in Figure 25.

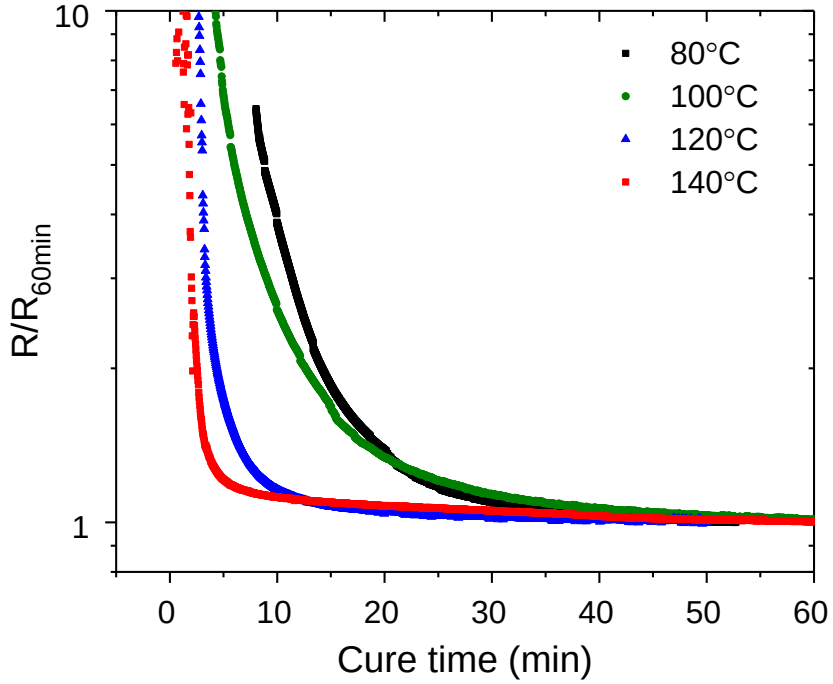

Figure 25. Resistance change during curing at 80°C, 100°C, 120°C, 140°C for about 60min

To reduce the variations between individual samples, the resistance during curing was normalized by using individual samples' respective R60 min, the resistance measured at 60 min. The infinitely large resistance at the onset of curing is because the silver NPs are surrounded and separated by solvent and organic shell, inhibiting the formation of a conductive path. The resistance changes show that the solvent evaporates gradually as a function of curing time, where longer curing times contribute to the drop in resistivity and the formation of conductive paths within wires. For the 120 °C and 140 °C cured samples, the resistance is nearly saturated within the first 10 min, which agrees with manufacturer suggested curing conditions, while the 80 °C and 100 °C cured samples show slower curing

rates, but the resistivity finally becomes constant after curing for 40–60 min. To calculate the resistivity, optical microscope images of the wire's cross-section were taken to measure the cross-sectional area (see Figure 22c for a typical image). Under the aforementioned printing conditions (15 psi pressure, 3 mm s^{-1} speed), the DIW printed silver wires had similar cross-sectional dimension, and had an average width of 1.07 mm, and a cross-sectional area of 0.062 mm^2. Using this measurement, the resistivity was calculated and is shown in Figure 26 for curing 60 min at different temperatures. The resistivity of bulk silver is also shown for comparison. With curing temperatures greater than 140 °C, the effect of temperature on resistivity is not obvious, and the saturated resistivity is ~8 times higher than that of bulk silver. In the lower curing temperature range (80 °C–120 °C), the resistivity drops significantly as the temperature increases. Interestingly, even at 80 °C, the ink can be conductive after being cured for 60 min, and the resistivity is only 5–6 times higher than those cured at 140 °C. In addition, Figure 25 shows that the resistance becomes almost constant after 40–60 min (even at 80 °C), indicating a wire with stable conductivity is formed.

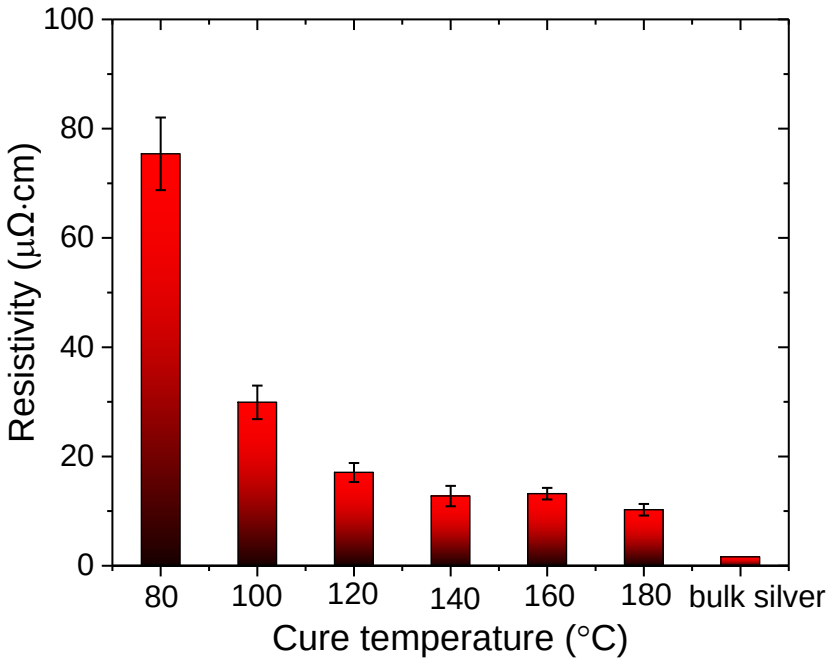

Figure 26. Calculated resistivity cured at different temperature for 60min and compared with bulk silver.

3.2.3 Microstructure Characterization

SEM images, in Figure 27, show the morphology and particle packing for the ink cured under different conditions. For comparison, images from the air-dried ink are also presented. The overall view (image in the middle) of the air-dried ink shows separated small islands with different shapes and diameters without a clear interconnected path. A zoomed-in image (the left image) of the connected area shows that the silver NPs of ~1 μm diameter are nearly separated from each other; for the unpacked area, small silver NPs having diameters of ~100 nm are separated from each other without forming a conductive path. In samples cured at 80 °C for 30 min, the formation of conductive paths can be seen.

As shown in the image in the middle, connected islands are forming, with some number of holes. The zoom-in of the connected area (left image) shows fully packed silver NPs and inter-particle boundaries can be seen but not very clearly. For the unpacked area (right image), large particles that are close to each other (as compared to the air-dried samples) are observed. When cured at 180 °C for 30 min, some pores exist, which might be responsible for the relatively large resistivity as compared to bulk silver, but large connected regions are also obvious. From the zoom-in of the connected region (left image), better connected particles can be seen; even in the not-fully connected-region (right image), silver NPs are physically in contact.

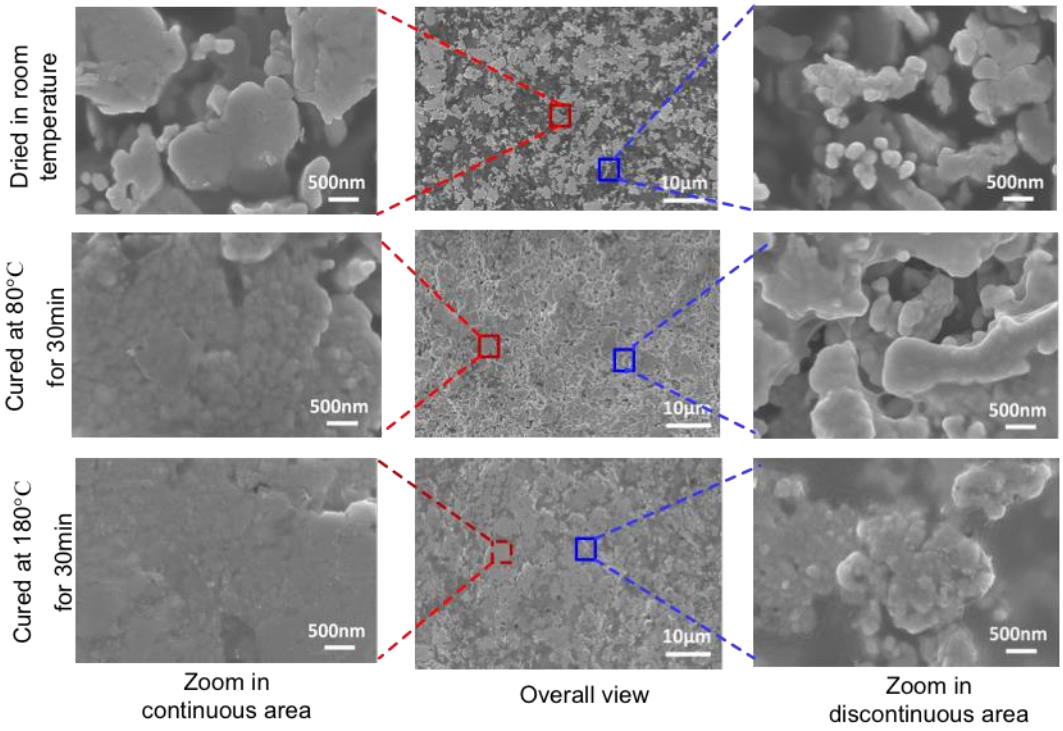

Figure 27. Comparison of SEM image of surface morphology: as dried, cured for 30 min at 80°C and cured for 30 min at 180°C.

3.2.4 Electro-Mechanical Properties

Tensile tests on freestanding silver wires, using the testing setup shown in Figure 23, were conducted. Three samples were tested for each curing condition. Figure 28 shows results from two representative samples subject to two different curing conditions (80 °C for 20 min and 140 °C for 20 min, respectively). The sample cured at a higher temperature exhibits a much higher yield stress and a lower yield strain than does the lower temperature cured sample. In addition, the resistance of the high temperature cured sample is more sensitive to strain during stretching than that of the low temperature cured one. Surprisingly the silver wire can be stretched significantly. For the sample cured at 140 °C for 20 min, the cured wire can be stretched ~150%, but results in a significant increase in resistance; the sample cured at 80 °C for 20 min cured can be stretched 300% with an increase in resistance roughly 400 times. For applications in Hybrid 3D Printing involving active structures and soft machines, the conductive materials should have (1) high electrical conductivity to achieve high-efficiency for the devices, (2) compliance that matches with the substrate, (3) high elasticity, and (4) an almost constant electrical conductivity under applied strain. In the following sections, the focus is concentrated on the conductivity, modulus, yield strain, elongation and reliability of the DIW printed silver wires.

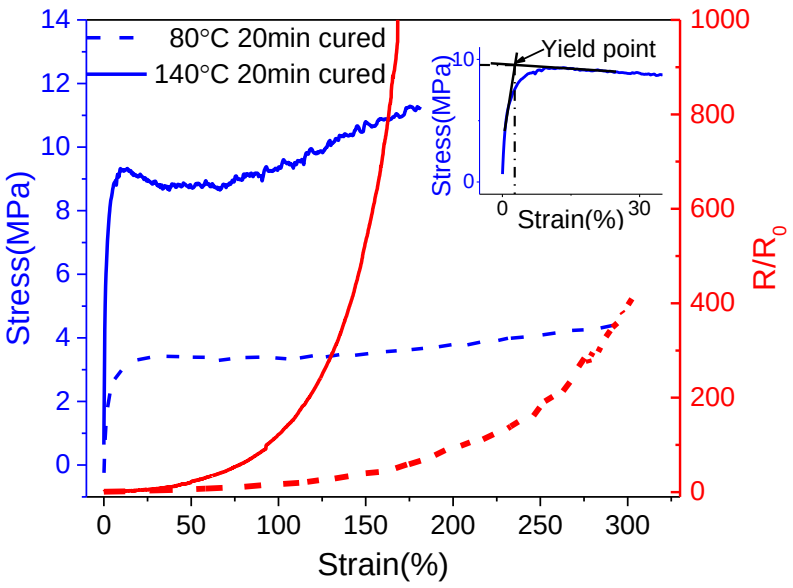

Figure 28. Stress-strain curves of printed silver wires and normalized resistance change when stretched, taking 80°C 20min and 140°C 20min cured samples as examples. The inserted image shows how to obtain yield strain and stress from the stress-strain curve of the 140°C 20min cured sample.

3.2.5 Conductivity

Based on the curing condition study (Figure 25 and Figure 26), curing conditions of the silver NPs was chosen to be in the oven at six different temperatures: 80 °C, 100 °C, 120 °C, 140 °C, 160 °C and 180 °C, with curing durations of 10, 20, 30, 40, 50 and 60 min; the results are summarized in Figure 30. In general, the resistivity decreases as the curing temperature and curing time increase. For the range of these curing conditions, the resistivity is between 150.9 and 10.2 μΩ cm, which corresponds to a resistivity of 94 and 6.4 times that of bulk silver (1.6 μΩ cm [22]), respectively. Since the 3D printed materials from the 3D printer can sustain a high temperature of ~120 °C, we chose the silver wire that was cured under the mild temperature (lower than 120 °C) to serve as conducting wires

for Hybrid 3D Printing applications. The temperature dependence of the electrical conductivity for conductive materials can be expressed by the following Arrhenius-type equation [23, 24], which was also used to describe the conductivity change of silver NPs during sintering [22]

$$\sigma = \sigma_{\text{con}} \cdot \exp(-\frac{E_g}{2k_B T})$$

where σ is conductivity, Eg is the energy barrier associated with electron hopping between conductive sites, kB is the Boltzmann's constant, T is the temperature, and σ_{con} denotes a constant. The above equation can be rewritten as follows:

$$\ln \sigma = \ln \sigma_{\text{con}} - \frac{E_g}{2k_B T}$$

This equation was used to fit the conductivity as a function of curing temperature with a fixed curing time, as shown in Figure 29. The fitted results of the Arrhenius type equation are summarized in Figure 31, where the energy barrier Eg is estimated to decrease from 0.3580 to 0.2677 eV as the curing time increases from 10 to 60 min; the pre-coefficient $\ln(\sigma_{con})$ is around 18.8.

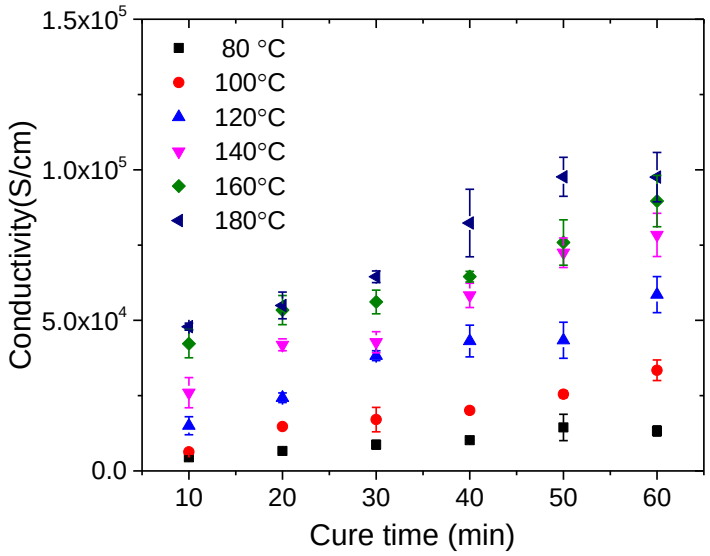

Figure 30. Conductivity variation of the silver conductive wires as a function of cure temperature and cure time.

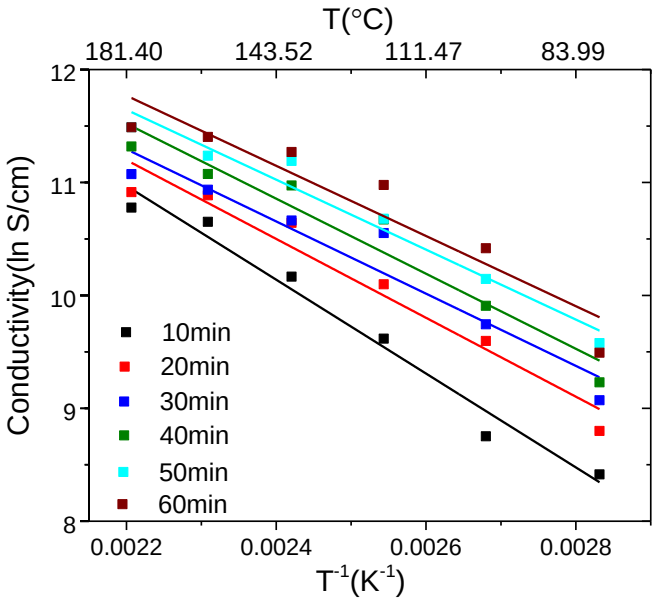

Figure 29. Arrhenius plot of electrical conductivity of Silver conductive wires

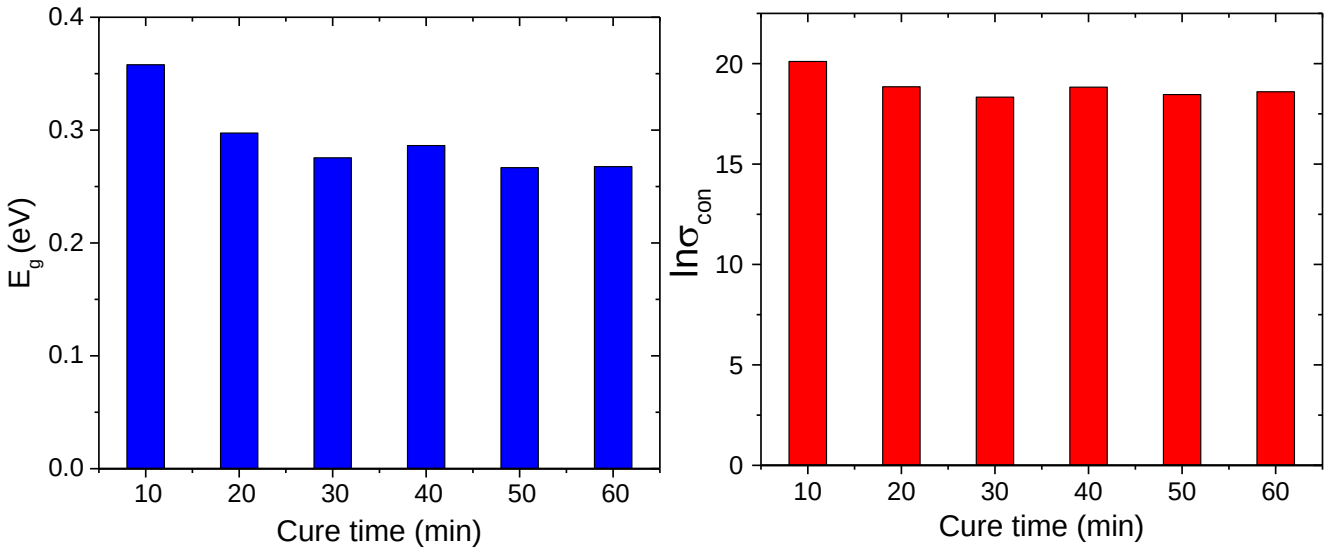

Figure 31. Eg and σ_{con} values estimated for different cure times

3.2.6 Young's Moduli

Figure 32 shows the evolution of Young's moduli as a function of curing temperature and curing time. Here, the Young's modulus is determined from the initial slope of the stress–strain curve (~0.5%). It is clear that a higher temperature, or a longer curing time, leads to a higher Young's modulus. This is consistent with the SEM observations that higher curing temperature yields to more compacted and better-connected silver NPs.

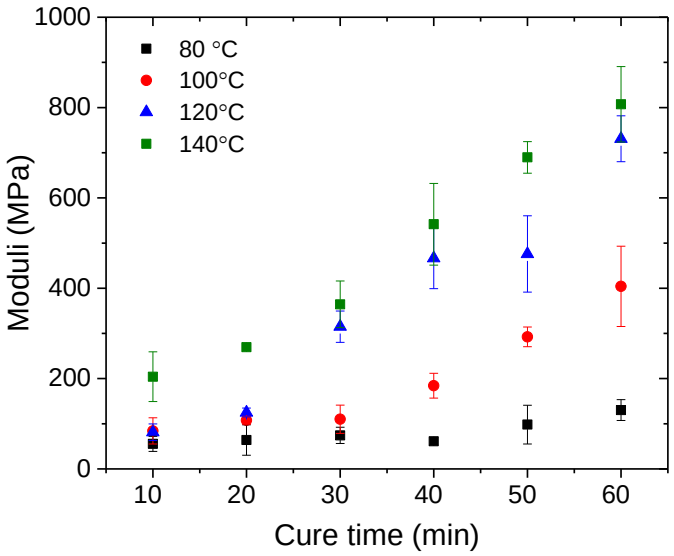

Figure 32. Modulus as function of cure time and cure temperature.

The Young's moduli, however, are lower than that of bulk silver. From Figure 32, the highest modulus is ~800 MPa, under the curing condition of 140 °C for 60 min. For bulk silver, the modulus of electron-beam deposited free stranding Ag films is roughly 63 GPa, and the calculated E ⟨111⟩ is 82.2 GPa [25]; inkjet printed silver film after being sintered at 250 °C has a modulus around 50 GPa [26]. It is also interesting to note that for the 80 °C curing temperature no significant change in modulus as a function of curing time are observed, even though this temperature yields a conductive line after curing. During these experiments, it was noted that curing temperatures higher than 140 °C resulted in wires that were very stiff, which significantly limited their ability to stretch. Therefore, in the following, samples with curing temperatures below 140 °C were used for the electromechanical property studies.

3.2.7 Yield Strain

The yielding point is determined from the intersection of tangents of the stress–strain curves to obtain the yielding stain and stress as the inset in Figure 28. The yielding strains and yielding stresses are summarized in Figure 33. The yielding strain decreases with an increase in curing time and temperature, while the yielding stress increases with an increase in curing time and temperature. In general, the cured silver wires have yielding strains between 2.0% and 9.4%, which is larger than freestanding metal film that can be stretched by only 1%–2% [27].

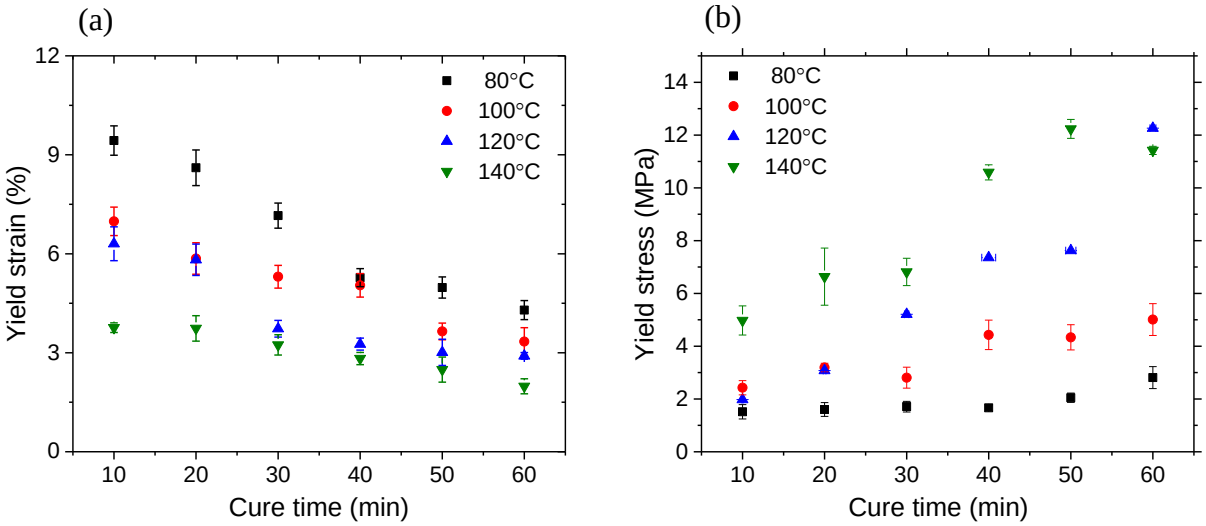

Figure 33. Yielding (point of intersection of tangents) behavior as a function of cure time and temperature (a) yielding strain; (b) yielding stress.

3.2.8 Elongation

As Figure 28 shows, the cured silver wires can withstand a large elongation. During the experiments, the resistance increased into the MΩ range when the wire was subjected to large strains (>300%). Here, for the sake of analysis, the ultimate elongation is defined as the strain when the normalized resistance is increased by 100 times (R/ R0 < 100) or the silver wire breaks and conductivity is lost, whichever occurs first. Figure 34 shows the ultimate elongation of wires cured under different conditions.

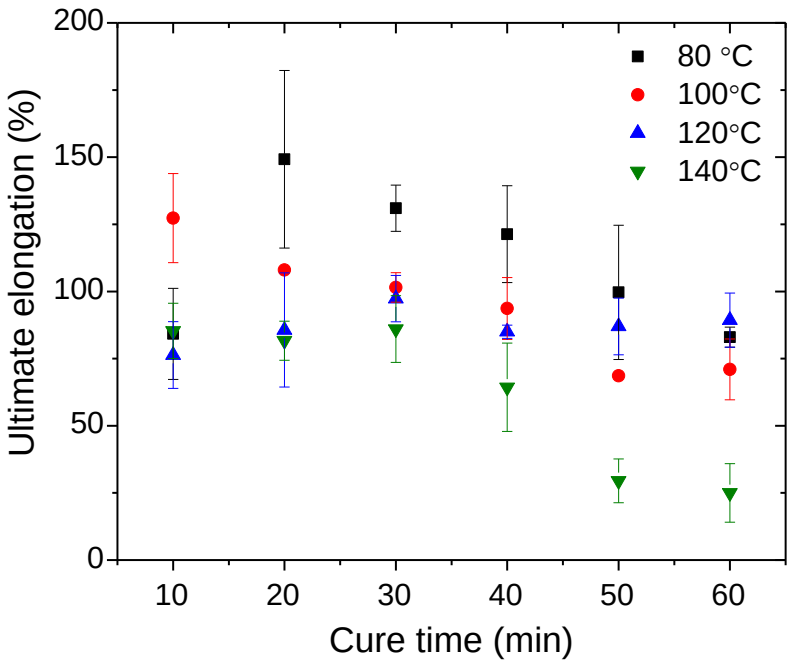

Figure 34. Ultimate elongation (R/R0 <100 or sample crack) as a function of cure temperature and cure time.

In general, the wires can obtain ~100% ultimate elongation for most curing conditions, which is much larger than sputtered metal films, which have a maximum elongation of around 50% on elastic substrate [28, 29] . This value is also larger than screen printed silver ink, which is about 50% [30]. Figure 34 also shows lower temperature cured silver wire has a longer elongation. In addition, 20 min curing time gives the largest ultimate elongation for all the curing temperatures. Figure 34 shows that the silver ink in this study is capable of large elongation. Therefore, if it is deposited on an elastic substrate it may achieve high elastic deformation and used for embedded printing [31], encapsulation [32], and other methods that have potential for stretchable electrodes application. In addition, the printed silver wires in this work cured at temperatures between 80 °C−120 °C for 10–30 min are suitable for stretchable applications and soft machine usage, which typically require moderate to large deformation of the substrate materials.

3.2.9 Repeatability

Maintaining a high conductivity of printed silver wire during cyclic stretching and relaxation is as important as obtaining high initial conductivity. Cyclic testing is widely used to measure the reliability of materials [33-36]. Here, the printed wires were loaded/unloaded in cycles using the DMA tester. In these studies, the samples were elongated and relaxed at 25 MPa min^{-1}; at the end of each cycle, the samples were left unloaded for 0.5 min to provide a strain relaxation period for the silver wire to recover. The changes in resistance was measured by using the multimeter and LabVIEW as previously demonstrated, in Figure 23. In addition, since the wires cured at 80 °C for 20 min can be stretched to the maximum amount while maintaining good conductivity, these wires were chosen for our cyclic tests. Figure 35(a) shows the cyclic stress–strain curves

for 100 cycles. Under the load control, for the first cycle the maximum strain is about 7.6%; after 100 cycles, the maximum strain increases to 16%. Therefore, after 100 cycles, the strain increases less than 10%, suggesting that there is about 0.1% average residual strain in each cycle. In Figure 35(b), the comparison of the stress–strain curves of 1, 2, 5, 10, 20, 50, and 100 cycles is shown; for the sake of clarity, the curves have been shifted so that they all start from the zero strain. Overall, the shape of the stress–strain curve only changes slightly. It can be seen that the hysteresis decreases after the first initial loading– unloading cycles, maintaining its value for the following 10 cycles, then the hysteresis increases gradually. The hysteresis might be due to the viscoelastic behaviors of the wire, where the recovery time is larger than the 0.5 min hold time in the experiments. The viscoelastic behaviors may come from the fact that organic components in the ink were not fully removed under the 80 °C for 20 min curing conditions. Figure 35(c) shows the evolution of the Young's modulus with the number of cycles. It can be seen that the modulus slightly increases in the second cycle, but has a decreasing tendency in the following cycles. Figure 35(d) shows the evolution of normalized transient resistance of the 80 °C 20 min cured silver wire during the loaded/unloaded cyclic test. Since in each cycle, the sample was stretched then unloaded, the normalized transient resistance oscillates in each cycle; the maximum R/R0 measured in the stretched state and the minimum R/R0 measured in the unloaded state increase slightly as the number of cycle increases. When allowed to relax at the released state, most of the resistance increase can be recovered. The maximum R/R0 measured in the extended state gradually increases from 1.1 to 1.6 in 100 cycles. The resistance at the strain minima also increases to 1.3 times the initial value after the 100th

unloading cycle. Using conductivity σ, which is the inverse of resistivity ρ, equation (1) can be rewritten as

$$R = \frac{l}{A}\frac{1}{\sigma}$$

let R be the resistance of the silver wire, which is stretched to length l and cross-sectional area A. Let R_0, l_0, and A_0 be the corresponding initial values. The dimensions of the sample change with strain, as expressed by

$$l = l_0(1+\varepsilon)$$

$$A = A_0(1-\upsilon\varepsilon)^2$$

where ε is strain, υ is Poisson's ratio (0.367 was chosen for silver [37]). The conductivity change of the silver wire during loading/unloading can be predicted by using equation (2),

$$\frac{\sigma}{\sigma_0} = \exp\frac{E_{g0} - E_g(\varepsilon)}{2k_BT}$$

where Eg0 is the energy barrier associated with electron hopping between conductive sites at the initial state of silver wire, Eg(ε) is the energy barrier during the experiment when the strain is ε, so the strain-dependent normalized resistance of silver wire can be predicted by

$$\frac{R}{R_0} = \frac{1+\varepsilon}{(1-\upsilon\varepsilon)^2}\exp\frac{E_g(\varepsilon) - E_{g0}}{2k_BT}$$

On the assumption that the conductivity σ of the silver wire remains unchanged, the normalized resistance change can be rewritten as

$$\frac{R}{R_0} = \frac{1+\varepsilon}{(1-\upsilon\varepsilon)^2}$$

The solid line curve in Figure 35(d) is the theoretical equation (9) (plotted as a function of strain, which is the top horizontal axis) and is calculated using the strain value at the stretched state. During the cyclic tests, the energy barrier Eg(ε) may increase, and resistivity will increase as a result. The cyclic loaded/unloaded tests were conducted by DMA stress control. The shift of strain was compared at 1, 2, 5, 10, 20, 50, 100 cycles under four different stress levels, corresponding to 2.1%, 7.6%, 9.2% and 19.1% maximum strain in the first cycle in Figure 35(e). The larger the strain in the stretched state, the larger the strain shift. In addition, the shift strain is not sensitive to the number of cycles when the applied strain is small (~7%) but strongly depends on it at high strain level (>9.2%). For the 9.2% maximum strain in the first cycle test, after 100 cycles the strain is about 100%, and for the 19.1% test the sample failed at 26th cycle. The normalized resistance change under different stress levels during the cyclic test were compared in Figure 35(f), the resistance changes have the same tendency as the shift of stain in Figure 35(e).

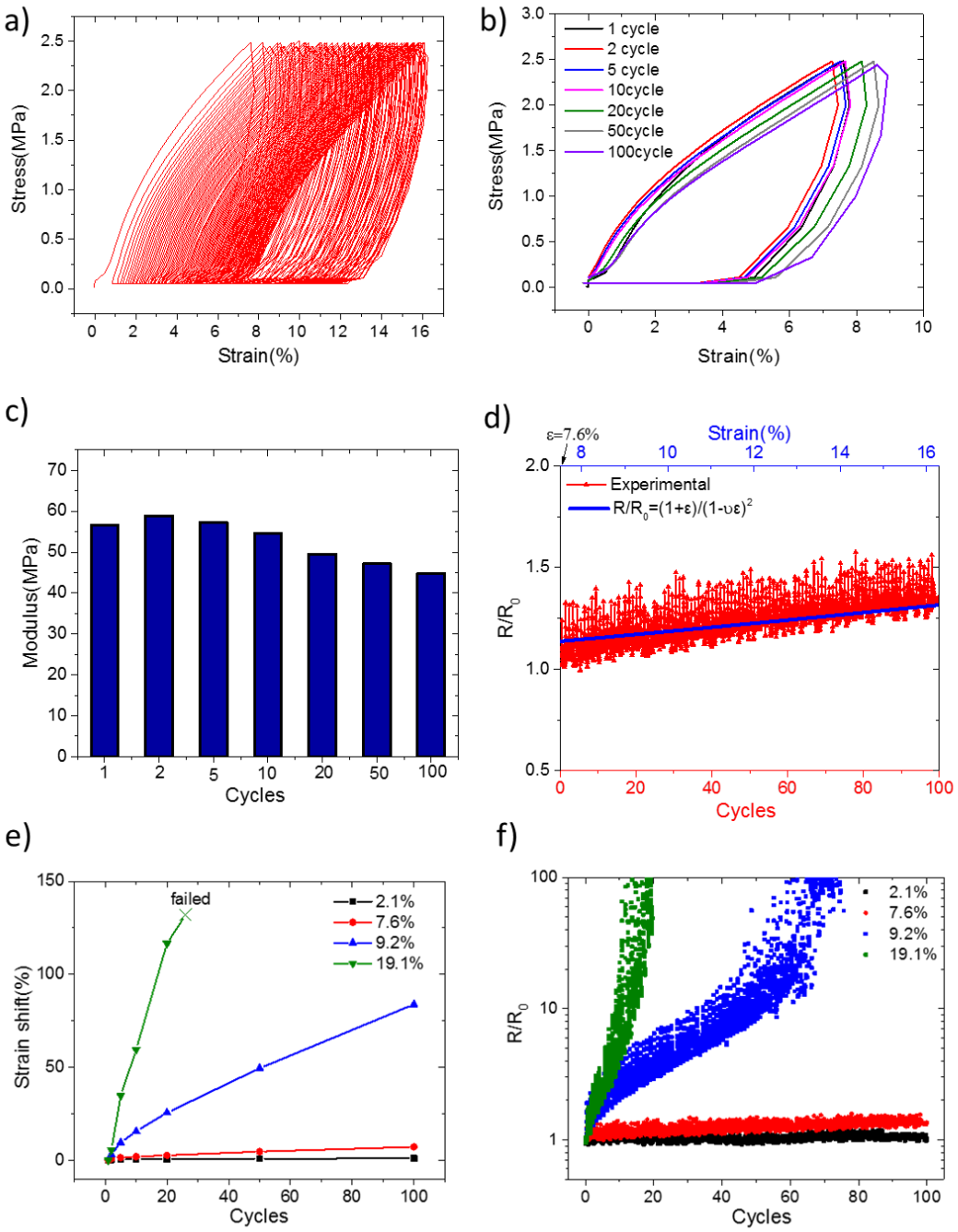

Figure 35. Repeatability of printed silver wire (a) Cyclic stress-strain curves of silver wire that conducted by 25MPa/min DMA stress control (~1.3%/s) hold for 0.5min during every cycle, repeated for 100 cycles. (b) Selection of 1, 2, 5, 10, 20, 50, 100 cycles, and normalizing the initial strain of each cycle to 0. (c) Modulus of selected cycles. (d) Normalized transient resistance change as function of repeated cycles. (e) Strain shift as function of initial strain and repeated cycles. (f) Normalized transient resistance change during cyclic loaded/unloaded test as function of initial strain and repeated cycles.

3.3 Summary

In this chapter, it has been demonstrated that by modifying the thermal curing conditions, the electromechanical properties of silver wires created by direct ink writing can be tailored for application specific purposes. From the results obtained regarding the electromechanical properties of wires cured under different thermal conditions it is found that as curing temperature and curing time increase the cured wires become more conductive but less stretchable. The silver wires cured at 80°C for 10-30min have conductivity >1% bulk silver, Young's modulus <100MPa, ultimate elongation up to 300%, and yield strain ~9 % proving to be good for applications that require stretchable electronics. The silver wires cured at 120°C for 10-20min have good conductivity and are sensitive to applied strain and can be good for sensing applications.

CHAPTER 4.

APPLICATIONS OF HYBRID 3D PRINTING

In this chapter, results from chapters II and III are combined to demonstrate the capabilities of H3D Printing and its applications in 3D Printing of functional devices. Printing technologies are integrated using different H3D printing approaches, including the multi-media platform and the silver ink studied is used to increase functionality in printed parts. Stretchable electronics are printed that combine PIP and DIW. The interface strength between two materials printed with DIW and inkjet is explored and how geometric interface design influences the interface strength. Soft robotic actuators are printed in a single process, simplifying traditional fabrication techniques. And lastly fully printed capacitor is printed within a 3D structure.

4.1 Stretchable Electronics

Based on the results regarding the electromechanical properties of the thermally cured Dupont 5043 material in Chapter 3, the ability to print stretchable electrical wires to fabricate stretchable electronics is investigated. Curing the printed silver wires at 80°C for 10-30min are highly stretchable (as much as 150% ultimate elongation) and thus can be used in stretchable applications. The wires cured 120°C for 10-20min yield good conductivity and are sensitive to applied strain and thus can be used in sensing applications. In the following two demonstrations of potential applications are presented[15].

4.1.1 Stretchable Ribbon Cable

A ribbon cable is a commonly used wire harness with applications requiring multiple signal or data lines condensed into a single cable. To replicate a ribbon cable a H3D printing process is used where a stretchable substrate material (TangoBlack, Stratasys Inc.) is printed with the Objet Connex 260 3D printer. The substrate is printed up to a certain level where the DIW printed silver conductive lines can be printed, creating individual wires. Once printed, the object is cured and then encapsulated by subsequent layers of TangoBlack. This process can be repeated to create multiple layers of embedded ink, resulting in a high density of wires within a thin cable. Here, a ribbon cable with eight conductive lines was printed and 4 LEDs were connected by manual insertion into the ribbon cable.

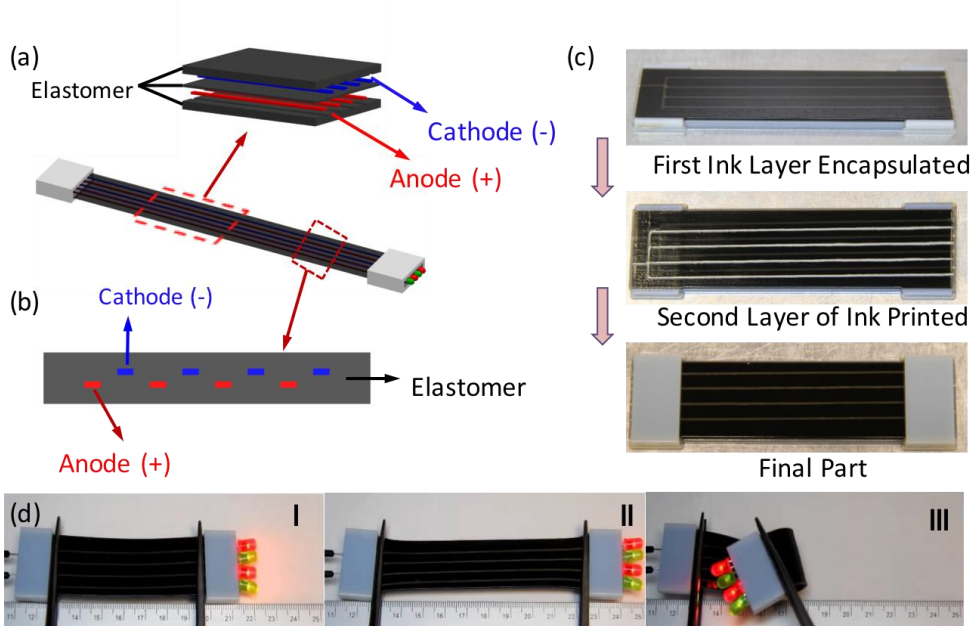

Figure 36. Fully printed stretchable cable by embedded silver wire into PolyJet 3D printed parts: (a) The design of the cable. (b) The cross-section of the stretchable part of the cable. (c) The images of the printed part during the printing process. (d) Embedded silver wires in elastomer as circuits during stretching. Images of the printed cable under tensile strain of (Ⅰ) 0% and (II) 40% and (Ⅲ) under folding.

The wires were cured under the same condition as the single LED ribbon cable. The printed ribbon cable was stretched as much as 45% while still illuminating the LEDs during testing, and is shown in Figure 36. The ultimate elongation of the cable is limited by the TangoBlack material as it will fail before the silver wires.

4.1.2 Soft Strain Sensor

To further demonstrate the capabilities of hybrid printing, a strain sensing ring was printed using the same approach as the ribbon cable. Here, a single serpentine strain gauge was embedded within a TangoBlack ring structure, shown in Figure 37. The ink was cured at 120°C for 20min, a suitable curing condition for sensing applications.

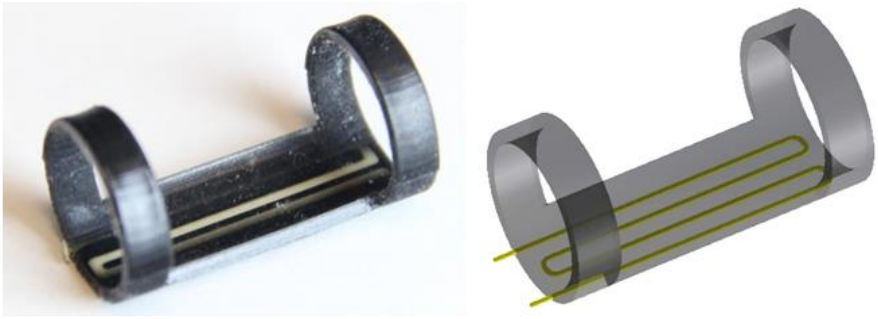

Figure 37. As printed and CAD representation of flex sensor

When the ring is placed on a finger and is subject to any bending, the silver strain gauge embedded on top of the ring stretches causing an increase in resistance. When the finger is relaxed the resistance decreases to it's nominal, as printed, value. The relationship between the bending angle and the resistance of the sensor was tested to directly determine the finger's state. Figure 38 shows the sensors sensitivity to applied bending. Curve fitting was used to give a mapping from resistance to bending angle for the sensor.

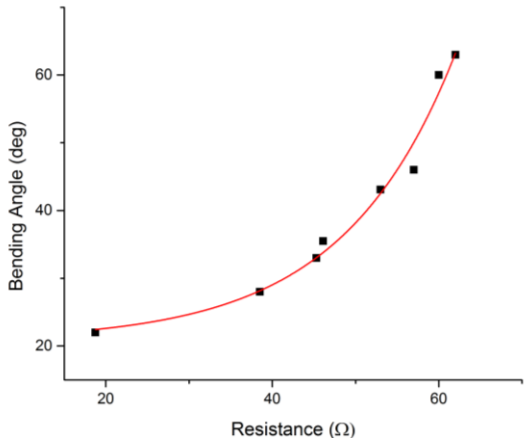

Figure 38. Calibration data for flex sensor, correlating resistance to bending angle

The ring sensor was tested under different bending conditions and the typical operation response can be seen in Figure 40. The sensor was tested under three bending configurations, 1) straight, 2) partially bent and 3) bent shown in Figure 39.

The sensor was tested by varying the bending frequency between two bending configurations. The sensor can detect bending between different configurations. The sensor exhibits a decay of the resistance while holding a bent state which can be attributed to stress

relaxation of the silver wires which exhibit viscoelastic behavior. The sensor reading can be filtered to remove the unwanted peaks in readings.

Figure 39. Images of a bending sensor on a finger-ring mounted on the forefinger, in straight (I) and bent (II and III) positions

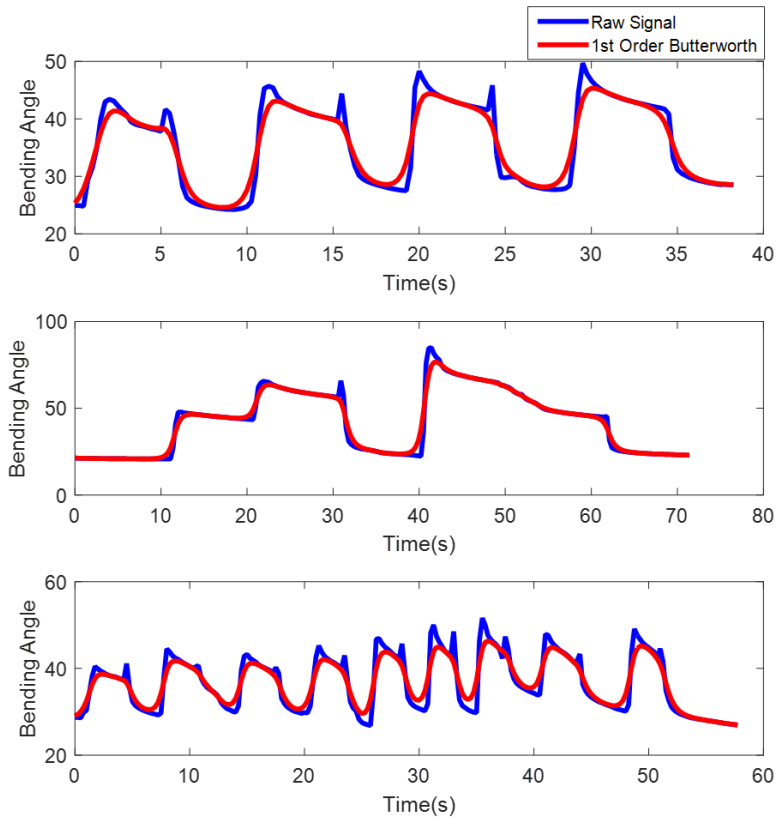

Figure 40. Raw and filtered changes in bending angle measured by the embedded silver strain sensor undergoing different bending tests.

4.2 Mechanically Heterogenous Structures

With the introduction of Hybrid 3D printing comes new unexplored areas of interest, one of which is highlighted here is the compatibility between dissimilar materials. The ability to print materials using multiple technologies in a single print introduces challenges in overall part resolution and structural integrity. In this section, the interface strength between two materials printed with inkjet and DIW technologies respectively is investigated and the effects of geometric interface designs are presented.

The mechanical properties of the two materials of interest was first studied. The inkjet material is a commercially available photocurable polymer, ETIJET ULX5832 (SunJet, DIC Inkjet Solutions) and the DIW photocurable acrylate based polymer. The DIW ink was prepared by dissolving polycaprolactone (PCL, M_n=70,000~90,000, Sigma Aldrich) in N-butyl acrylate (BA, Sigma Aldrich) at 70 ^oC followed by mixing with the same amount of Ebecryl 8413 (AUD, Ebecryl 8413, Allena), i.e. with BA/Ebecryl 8413 of 1/1 (wt./wt.). The amount of PCL is about 0.8wt % of the total weight. Then 5wt% of fumed silica nanoparticle (Sigma Aldrich) was gradually added into the above mixture and stirred manually until a transparent blend was obtained. Finally, 1.5 wt. % of Diphenyl(2,4,6-trimethylbenzoyl) phosphine oxide (TPO, Sigma Aldrich) to the total mass was added and dissolved into the mixture.

Figure 41 shows the results from tension tests performed on 50x10x1.5mm (nominal dimensions) samples of the printed materials. Tests were performed on an MTS at a strain rate of 50mm/min. The Youngs Modulus of the inkjet and DIW materials are 200 and 0.6

MPa respectively. The DIW material is a soft and highly stretchable material, up to 475% strain at break, while the inkjet material is a stiffer with only up to 16.8% strain at break.

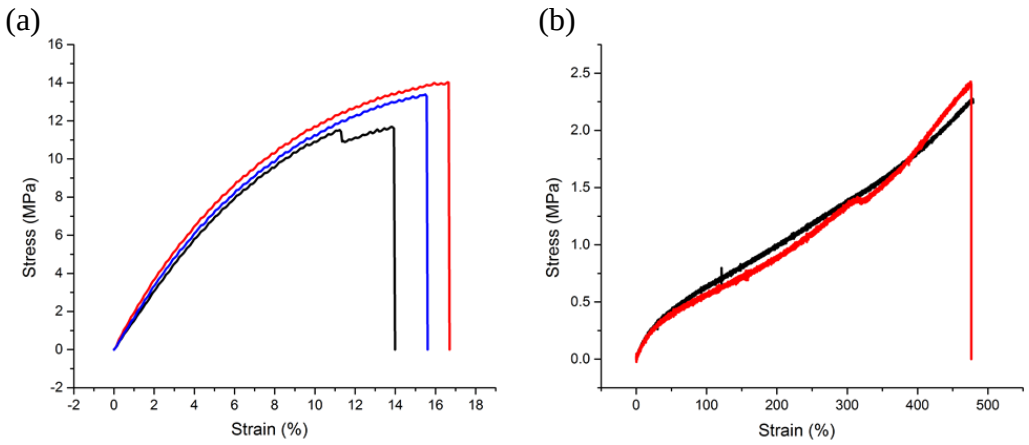

Figure 41. Tension Test of (a)Inkjet and (b) DIW materials

Dynamic mechanical analysis (DMA) was also conducted on a TA Q800 DMA (New Castle, DE, USA) using a tension clamp to get an understanding of the thermomechanical properties of the materials. The samples were heated from -30 to 120 °C with a heating rate of 3°C/min. The oscillation aptitude is 20.0 um. The static force is 0.01 with the force track of 125%. From Figure 42 the glass transition temperatures observed from the $\tan\delta$ peaks of the Inkjet and DIW materials are -4.5°C and 64.5° respectively. The inkjet material exhibits a relatively wide $\tan\delta$ peak indicating the glass transition of this material occurs over a temperature range, rather than a well-defined temperature. The high T_g of the Inkjet material allows for use in shape memory polymer printing, although the shape fixity is will

not be very high. The DIW material is a rubber like material with low rubbery modulus around 0.6MPa.

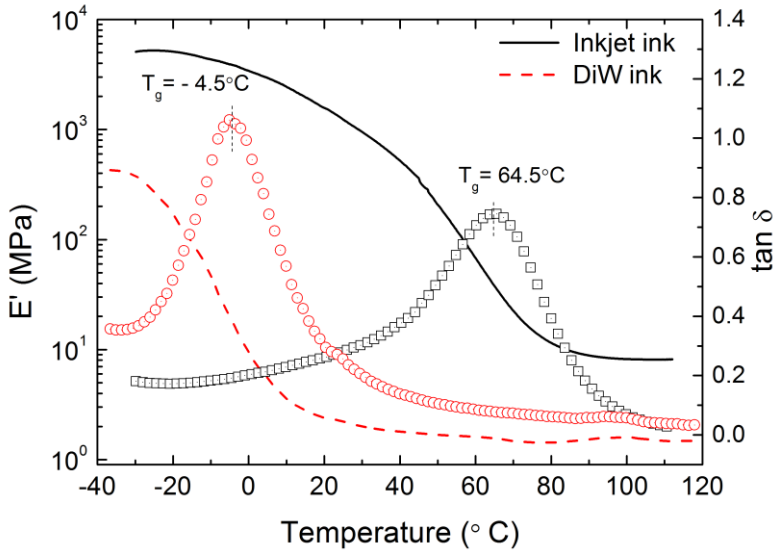

Figure 42. Dynamic Mechanical Analysis of Inkjet and DIW materials

To print the two materials together a printing scheme was developed, where multiple inkjet layers are printed to a height that is equivalent to the layer thickness of a single layer of the DIW printed material. After the inkjet layers have been printed the build tray moves under the extrusion module where a layer of DIW material is printed and then returned to the inkjet module and cured under the UV lamps. This process is repeated as many times as required for the part to be fabricated.

The interface between the two materials was studied by printing different interface geometries between the materials and preforming tension tests of the printed samples. Three interface designs tested were, a blunt, a buzzsaw and a lap joint and are shown in Figure 43. The blunt interface has no geometric alterations and simply consists of two

rectangular sections butted together. The buzzsaw interface is a pattern of interlocking triangular elements protruding from each half. And the lap joint interface overlays the two materials in equal portions where the cross section is split equally between the two materials.

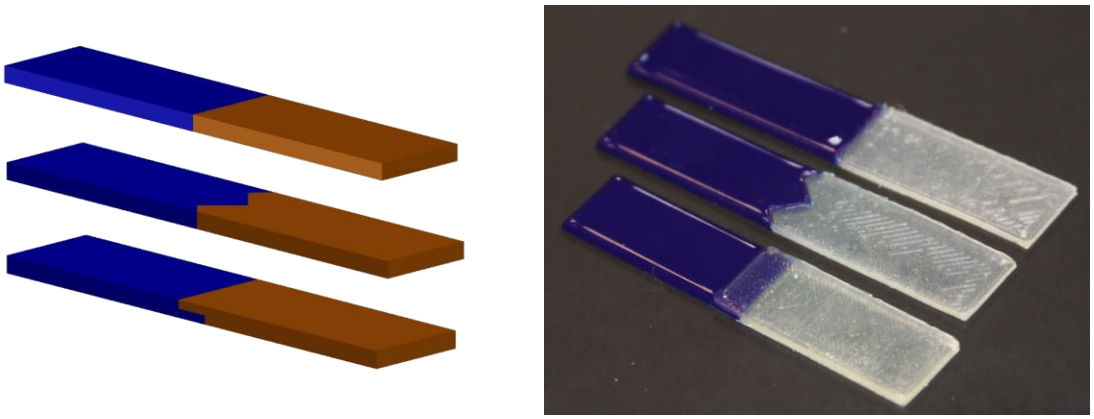

Figure 43. CAD representation and printed parts with different geometric interfaces.

Tension tests of each as printed parts were conducted, along with tension tests where an incision of various depths was made at the interface of the two materials. Results for the blunt interface indicate the as printed part could withstand up to 345% strain and can be seen in Figure 44. When incisions were made, the samples failed at much lower strains, 160% and 105% for 1.2mm and 0.5mm incisions respectively. The larger the incision the smaller the deformation the samples could withstand.

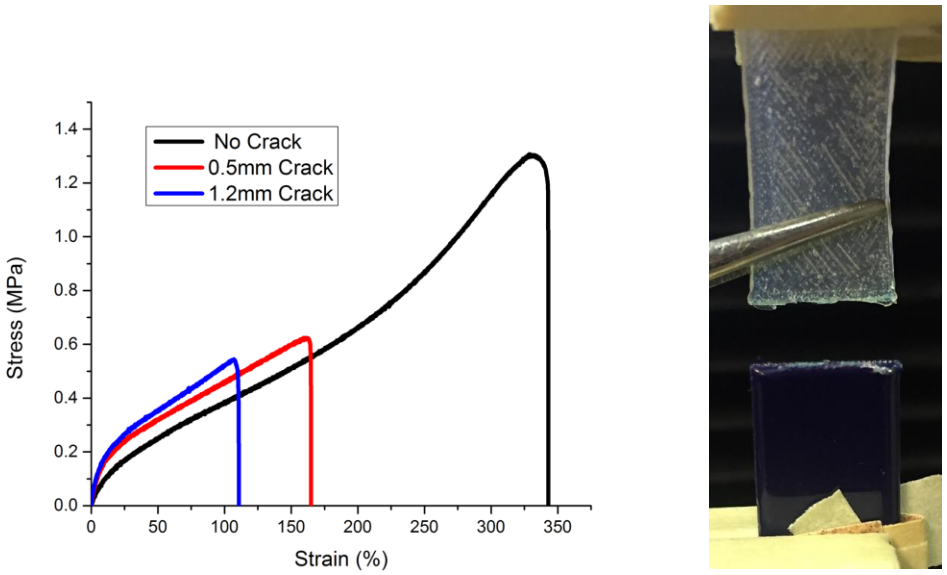

Figure 44. Interface strength under tension of Blunt interface geometry

The Buzzsaw interface decreased the interficial strength between the two materials, shown in Figure 45. Samples printed with the buzzsaw interface without incissions were not able to be stretched by more than 190%, only 40% of the strain handles by the bulk DIW material. Interestingly when incissions were made at the interfaces, the ultimate elongation did not change drastically. The strain at break was 140% and 220% for the 0.5 and 1.2mm incisions respectively. The incisions were not as big a factor for the buzzsaw as previously seen in the blunt interface. Here the geometric design of the buzzsaw creates stress concentrations at the points of the intersections, resulting in rupture between the two materials.

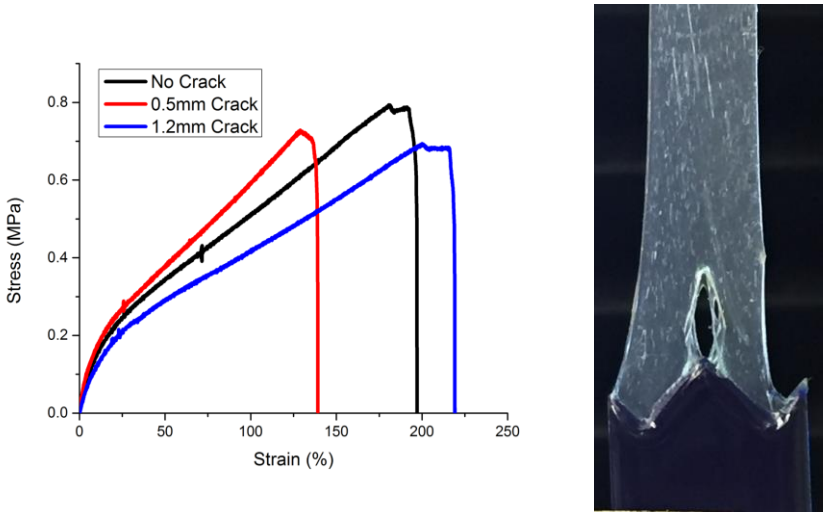

Figure 45. Interface strength under tension of Buzzsaw interface geometry

The last interface tested was the lap joint interface, which was able to withstand 145% at break for the as printed interface, shown in Figure 46. The joint without incisions resulted in a stiffer resonse than those with incissions that were able to withstand 165% and 130% strain at break for a 0.5 and 1.2mm incission at the interface respectivly. Similar to the buzzsaw interface, the lap joint was only able to withstand much smaller strains than the pure material, only 32%, and was not significantly affected by the incisions made. The lap joint fractured at the middle interface between the DIW and inkjet material where the sheer stress was maximized.

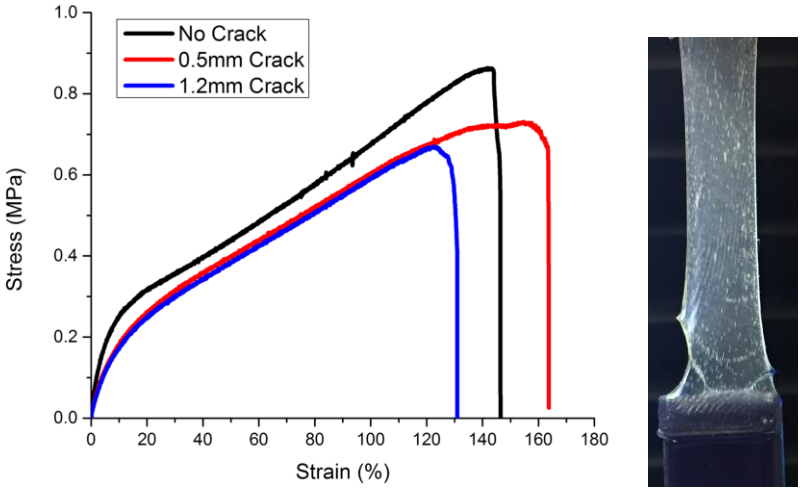

Figure 46. Interface strength under tension of Lap Joint interface geometry

When comparing the results of tesnion testing of the as printed samples it is obvious that the blunt interface provided the best interface strength of the interface geometries tested, shown in Figure 47. The blunt interface, without incisions was able withstand up to 345% strain at break, roughly 80% of the strain at break of the pure as printed DIW material, while the buzzsaw and lap joint interfaces were only able to withstand 40% and 30% of the strain at break of the pure printed DIW material respectively.

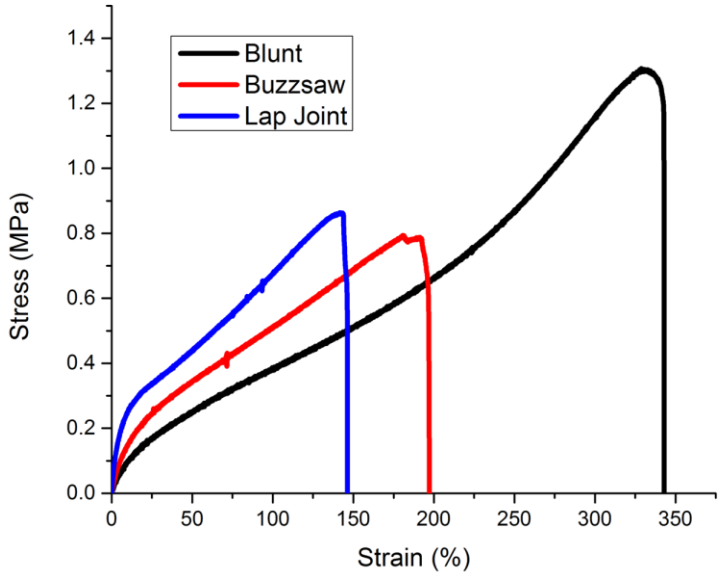

Figure 47. Comparison of interface strength of various interface geometries

From these results involving the strain at break between the two material, parts were printed to demonstrate both the H3D printing capabilities and utilize the highly stretchable DIW ink unable to be printed with polyjet technologies. For demonstration purposes a racecar wheel was printed with the interior spokes and rim made from the inkjet material and the tire from the DIW material. The wheel was printed in the same fashion as the interface testing samples, alternating between DIW and PIP during a single layer of printing. The wheel was designed to have a hollow, enclosed cavity in between the tire and wheelwell, like a traditional car tire, which is designed to be inflated to different pressures after printing, shown in Figure 48.

Figure 48. Car wheel replica Hybrid 3D printed with Inkjet and DIW materials

4.3 Soft Robotics

Soft robotics was traditionally a term used to describe robots with ridged links and mechanically compliant joints with variable stiffness. Recently the area of soft robotics has shifted form rigid links to bioinspired continuum robots that are “inherently compliant and exhibit large strains in normal operations”[38, 39]. Lots of work has been put into this area but fabrication techniques of soft robots are constrained by time consuming and labor-intensive fabrication processes involving the formation of complex, multiple piece molds

by either 3D printing or traditional techniques and complex embedded casting or soft lithography. 3D printing has enabled the ability to easily print complex mold geometries that improve the fabrication process, but the potential to use 3D printing to completely print soft robots has yet to be explored, from CAD to part in a single process. Here completely printed soft pneumatic actuators are presented, based on the design of previous work in the Whiteside's Research Group[40], using a hybrid printing approach. The actuators consist of a layered structure with an extensible top layer and a flexible, inextensible bottom layer. Between the top and bottom layers are hollow chambers which can be pressurized and results in expansion of the top layer. The shape change results in the structure bending due to the difference in compliance of the two materials [40]. The design of the actuators and schematic of the working principle is illustrated in Figure 49.

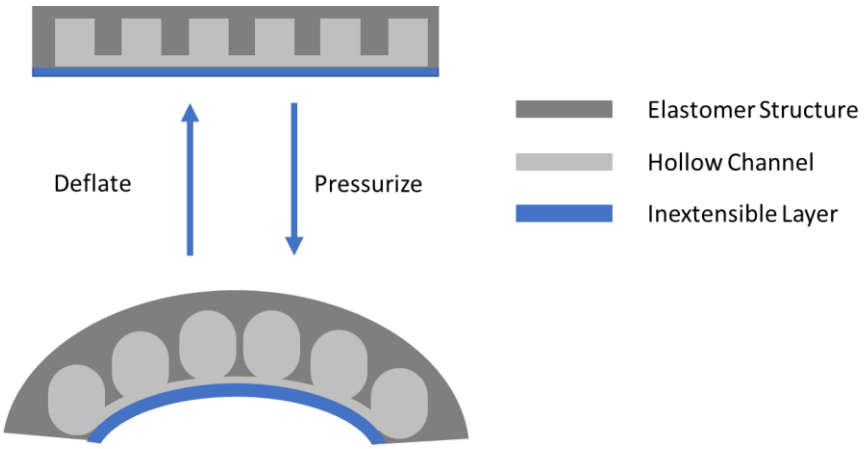

Figure 49. Cross section schematic of soft pneumatic bending actuator

A single bending actuator was first printed by combining IPJ and DIW printing methods. The materials used are the same used in section above. The inkjet ink acts as the inextensible material that enables the bending and the DIW elastomer is the extensible material used for the rest of the structure. The actuator was printed in a layer by layer fashion, switching between IJ and DIW printing modules in each layer. The printed actuator can be seen in Figure 50, along with the CAD representation.

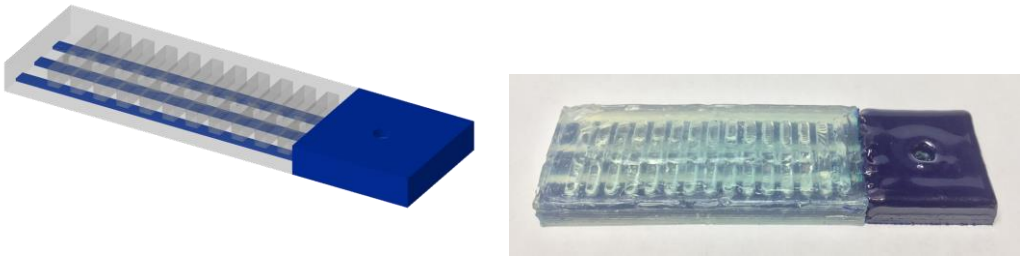

Figure 50. CAD representation and optical image of Hybrid 3D Printed pneumatic soft actuator

After printing the actuator can directly be pressurized to induce bending. A syringe is inserted into the printed inlet hole in the inkjet material and pumped to inflate the hollow inner cavities, shown in Figure 51. The soft material expands but is restricted by the stiff inkjet strips on the bottom half causing bending toward the inextensible material. The DIW material is expanded, causing bulging in some areas along the upper surface. The protrusions can be the cause of weak interfacial layer bonding in some areas or debris restricting the flow within the channels.

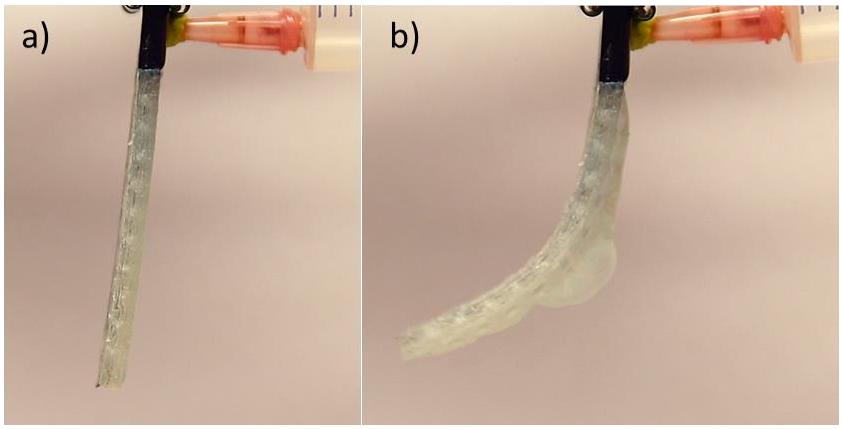

Figure 51. Pneumatic soft actuator a) deflated and b) pressurized

A more complex griper was also printed to showcase the complexity of objects that can be easily printed with the hybrid printing approach. The gripper consists of four fingers with similar geometries and structure as the single actuator. The actuation of the gripper is controlled from a single input port and pressurizes all channels together, shown in Figure 52.

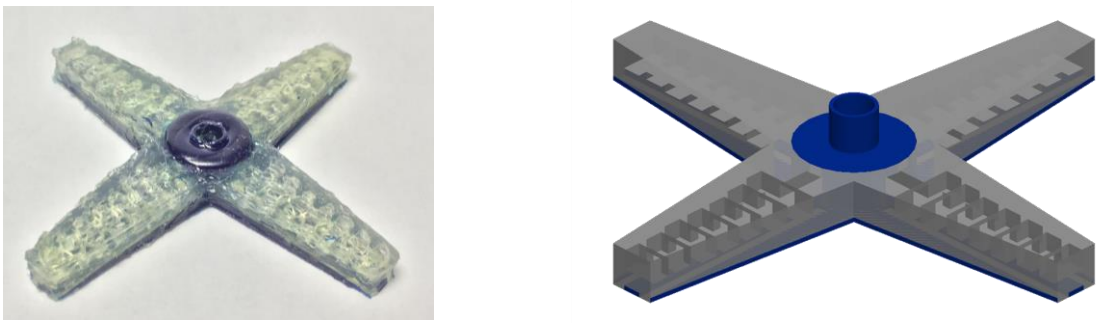

Figure 52. CAD representation and optical image of Hybrid 3D printed pneumatic soft robotic claw gripper

4.4 Smart Structures

4.4.1 SMP Recovery

Shape memory polymers (SMPs) are a subset of active materials which can retain a temporary shape and respond to external stimuli by changing their configuration back to a permanent shape. Often the stimulus that induces the recovery behaviour is temperature. A typical shape memory cycle follows a process that takes a glassy material at room temperature and heats it above the materials glass transition temperature (T_g) and is deformed while in a rubbery state. While holding the deformation the material is cooled back down, below the T_g, and the external load is released, resulting in a temporary (programmed) shape. This temporary shape can be maintained until the material is heated above its T_g causing the material to recover to its original shape. This shape memory cycle is illustrated in Figure 53.

Shape memory polymers on their own provide interesting areas of research from self-folding structures and devices[16-19, 21, 41], however, they rely on a thermal stimulus to induce recovery from a temporary shape that is typically introduced by means of placing

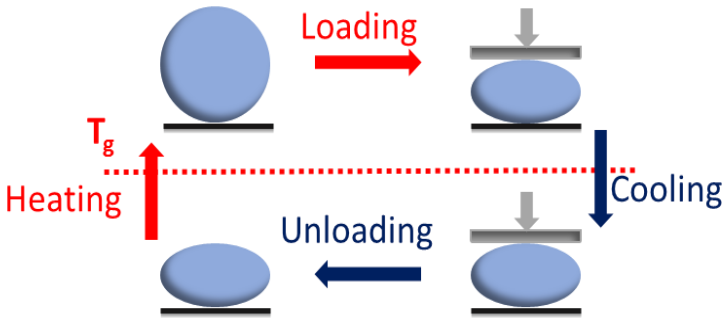

Figure 53. Schematic diagram of the shape memory cycle

objects in hot water or an oven, resulting in uniform heating of the entire structure. The ability to embed heaters within SMP structures offers the ability to induce recovery at specific locations and can be precisely controlled. Here, Hybrid 3D printing is introduced as a convenient and simple fabrication process. Silver is printed in channels of an inkjet printed SMP coin structure then fully encapsulated, creating a functional heating element able to be controlled with an external power supply. Figure 54 shows the fabrication process, from the SMP structure with channels, the silver printed in the channels and the final part. Thermal images show the temperature distribution as the heating element is powered. The coin demonstrates the shape memory cycle, shown in Figure 55, by first applying an electric field across the heating element bringing the sample above the it's glass transition temperature. When the sample has reached a high enough temperature, external loading is applied to deform the coin and the power supply is disconnected, allowing for the coin to cool down, while the load is fixed. After the coin is cooled to room temperate the external load can be removed and the coin can maintain its temporary deformed shape.

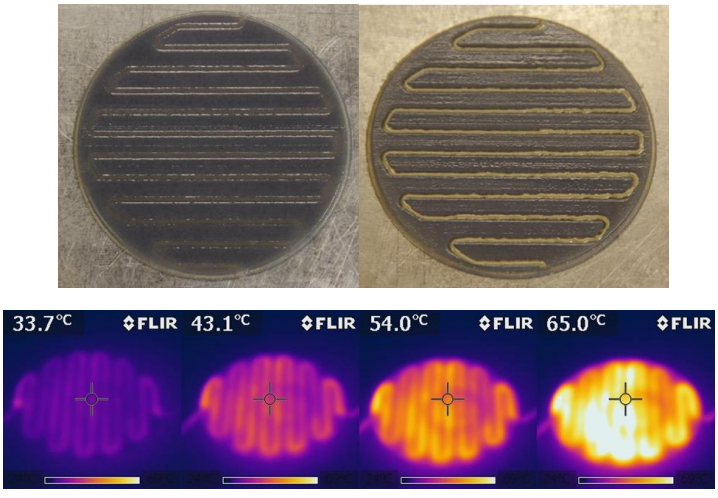

Figure 54. Optical images of 3D printed SMP coin with channels and printed silver heating element, with thermal images during the activation of the heating element

The coin can be returned to its original/permanent shape by simply powering the heating element and heating the coin above the glass transition temperature.

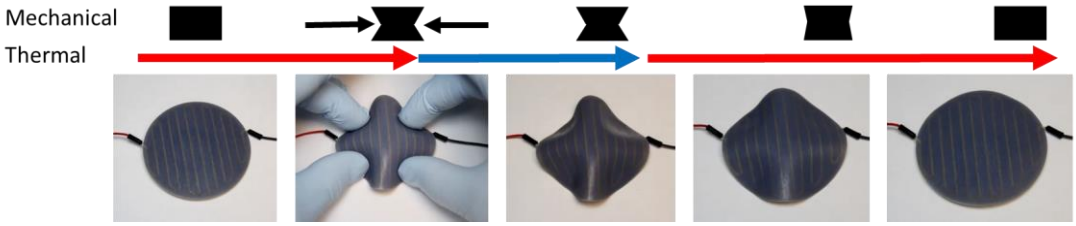

Figure 55. Images of the printed coin progressing through the shape memory cycle

4.5 Embedded Electronics

In this section, two demonstrations of embedded electronics are presented, one where a chip LED is placed inside a 3D printed structure with the robotic arm during printing and the other where a capacitor is printed within a 3D printed structure.

4.5.1 Digital LED Lamp

The flexibility of the printing platform allows for the integration of electronic components within a 3D printed structure, with the help of the robotic arms. Here a digital LED lamp is fabricated by printing a base structure with FDM. The base structure is an ABS rectangle with a hollow pocket and connecting channels for the Lohas 50W chip LED and printed silver electrodes respectively. Figure 56 shows a cross section schematic and CAD

rendering of the printed part with the three components, the abs structure, silver ink wires and the chip LED.

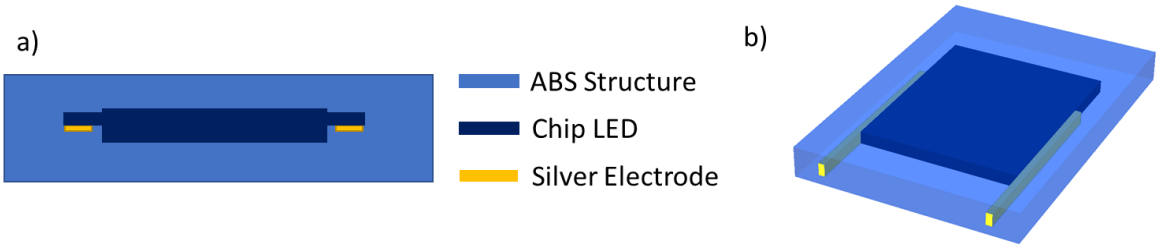

Figure 56. Digital LED lamp a) cross section and b) CAD rendering

The FDM structure is first printed up to a defined layer with the channels and pocket exposed (Figure 57(a)), then silver ink is printed in the channels for connections to the LED and an external power supply. After the silver has been printed the printing platform moves over to the robotic arm with an LED on the printing platform. The robotic arm performs a single pick and place routine that places the LED into the vacant pocket of the FDM structure Figure 57(b). After the pick and place the LED terminals lie on top of the printed silver wires, creating a good connection before the ink is cured. The part then moves back to the extrusion module where the LED is encapsulated using the FDM printhead Figure 57(c). The ink is partially cured during printing with a heated platform (~80°C) and then post cured in the oven at 100°C for 20 minutes. The final printed part is shown in Figure 57(d).

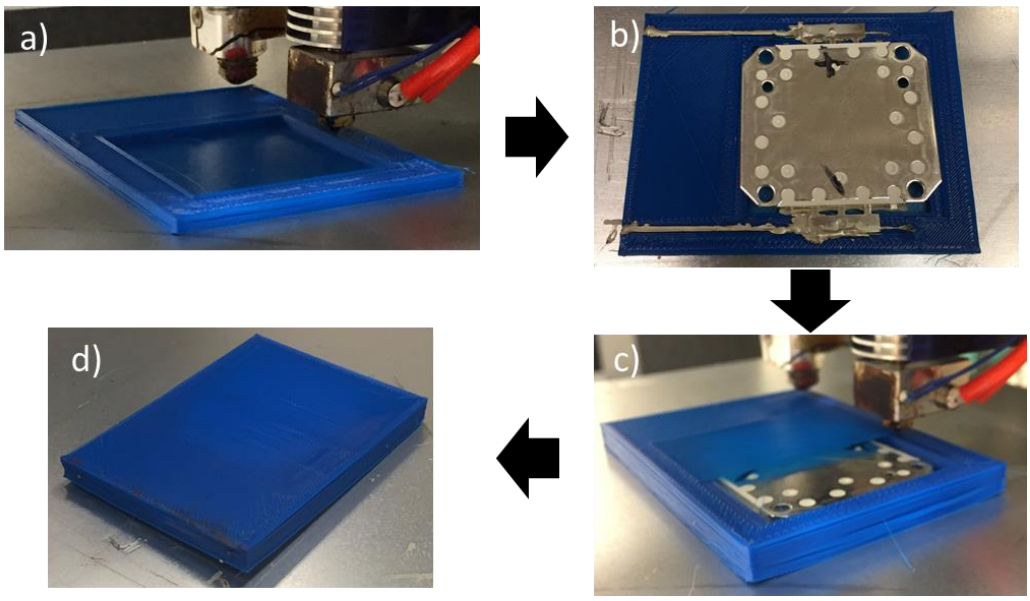

Figure 57. Integrated printing process of embedded chip LED. a) FDM printed structure with pocket for LED, b) silver wires printed with chip LED placed in the pocket, c) FDM printing encapsulating the LED and silver wires, d) fully encapsulated device.

After the part has been printed, external wires can be inserted into the channels containing the printed silver electrodes for connections to an external power supply. A power supply is used to directly power the LED and controlling the voltage and current can turn the light on and off as demonstrated in Figure 58.

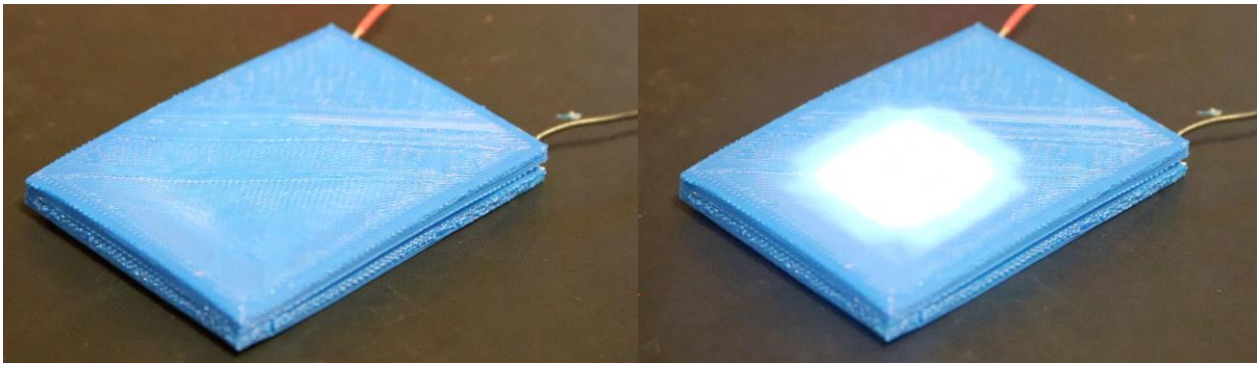

Figure 58. Functional printed digital LED lamp

4.5.2 Fully Printed Capacitor

Traditional methods for fabricating electronics is to solder components, such as integrated circuits (ICs) or passive components, onto a ridged printed circuit board (PCB). The potential to manufacture electronics by means of additive manufacturing can prove advantageous in regards to the simplicity and costs [42]. A capacitor is a common electronic component used to store an electric charge and can be found in most electronic devices. Here, the concept of Hybrid 3D printing is used to fabricate a fully printed capacitor. Inkjet Photopolymer Jetting and Direct Ink Writing are combined in a single printing process to fabricate the capacitor. IPJ is used to print the substrate and the dielectric material of the capacitor. The previously studied silver ink from DuPont is used as the electrodes. The capacitor electrodes are designed as a network of interlocking comb patterns connected in parallel to maximize the surface area of the plates while keeping a fixed plate distance in an effort to increase the overall capacitance. The printing of the capacitor involves the inkjet printing of the substrate material with a defined thickness, followed by the DIW of the silver electrodes leaving small gaps between the electrodes (Figure 59(a)). The nominal dimensions of the capacitor plates are 25x0.2mm with a plate spacing of 100μm. After the electrodes are printed they are encapsulated by inkjet printing and the void spaces left between the electrodes are filled in with the inkjet material and acts as the dielectric of the printed capacitor, Figure 59(b).

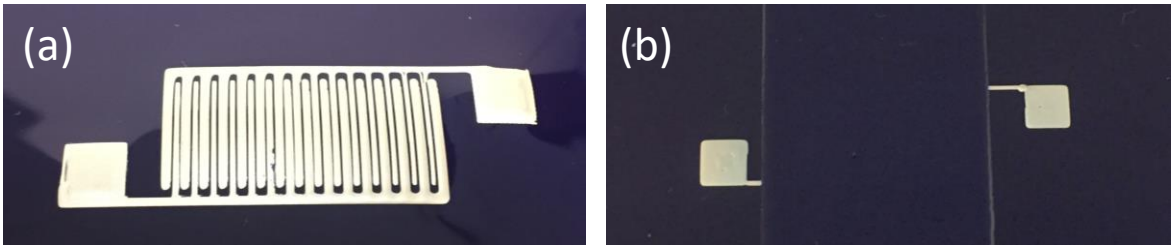

Figure 59. Hybrid 3D Printed capacitor with (a) silver interlocking comb electrodes and (b) the final capacitor with inkjet material enclosing the electrodes

After the capacitor has been printed, the sample is put in the oven at 110°C for 25 minutes to cure the silver ink. The capacitance of the printed sample was tested with an LCR meter (LCR-600 Global Specialties) and was measured to be 55pF. The capacitor was used in an RC low pass filter, Figure 60(a), connected to an external resistor and power supply to demonstrate a possible application. The external resistance was varied to demonstrate the tuning of the cutoff frequency defined at -3dB. The voltage measured across the capacitor, v_{out}, with a 1kΩ resistor used in the RC circuit is plotted with the applied square voltage waveform of amplitude 1V at 80Hz, v_{in} in Figure 60(b). The capacitor voltage, v_{out}, does not exhibit any phase lag and is not significantly attenuated. The frequency response of the RC circuit with varying external resistance values was analysed and the resulting Bode plots can be seen in Figure 60(c). From this figure, we can observe that as the resistance increases the cutoff frequency starts to shift to lower values. The cutoff frequency of a lowpass RC filter is defined as,

$$f_C = \frac{1}{2\pi RC}$$

and with a set capacitance of 55pF the cutoff frequency is solely dependent on the resistor and increasing the resistance causes a decrease the cutoff frequency.

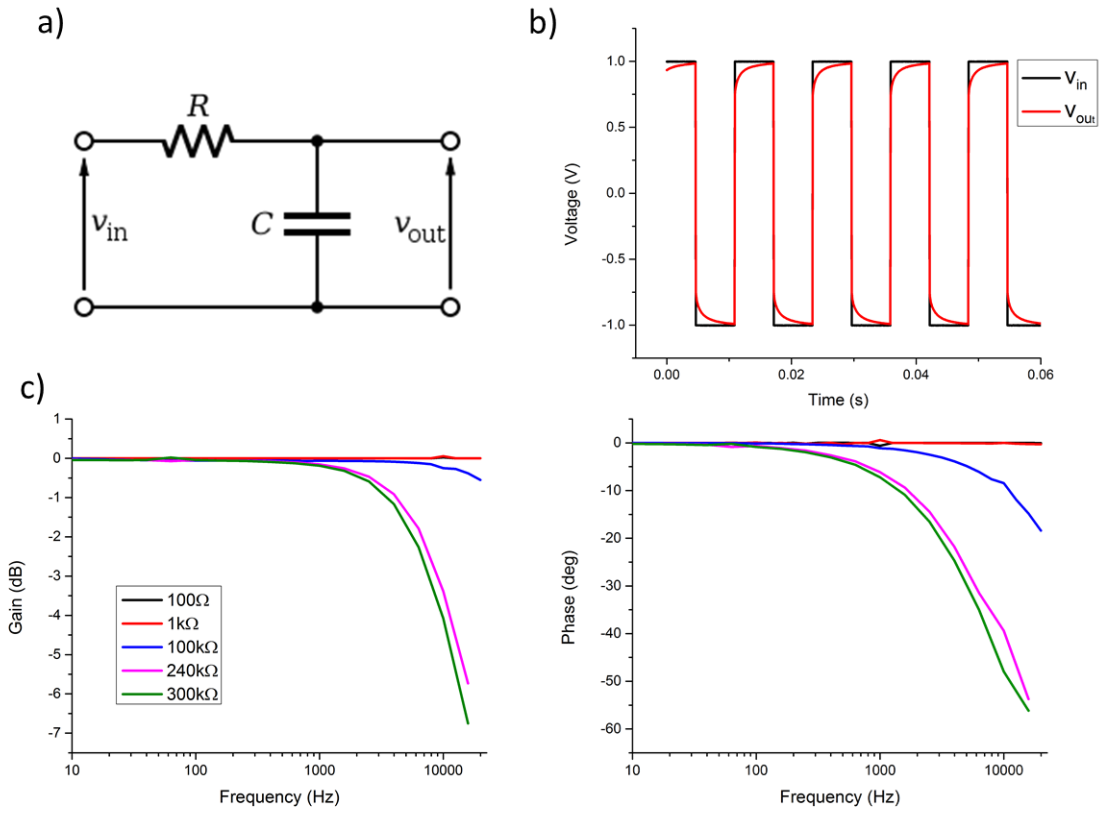

Figure 60. Experimental results of the capacitor used in (a) RC low pass filter circuit. (b) The input and output voltage at low frequencies shows little attenuation. (c) Frequency response of the RC filter with varied external resistance

The printed capacitor shows potential for use in electronics applications and the capacitance can be varied by changes in the electrode design. To better improve the capacitance without a large increase in the form factor of the device, a more suitable dielectric material with higher dielectric constant ε should be used, but never the less the printed capacitor demonstrates the feasibility of printed electronics within 3D printed objects.

4.6 Summary

This chapter builds upon the previous work presented in this thesis. The demonstrations in this chapter present some possible applications of Hybrid 3D Printing and show the potential for a range of applications. Stretchable electronics, including a stretchable ribbon cable and soft flex sensor, are fully printed using a H3D printing scheme. A study into the interfacial strength between two materials printed with different printing technologies and different interface geometries is presented and provides a baseline for printing structures with the two materials including soft pneumatic actuators. And lastly two examples of embedded electronics are presented that mix different printing technologies and robotic pick and place.

CHAPTER 5.

SUMMARY AND CONCLUSIONS

In Chapter 1, the idea of Hybrid 3D Printing was introduced alongside traditional additive manufacturing technologies while highlighting the potential realization of H3D printing. The work presented in this thesis provides the framework for which H3D printing can become common practice. A platform equipped with several AM and processing technologies has been designed and developed, with the big picture of enabling design freedom and expanding the scope of additive manufacturing. Chapter 2 details the design and fabrication of an integrated multi-media platform comprised of Aerosol Jetting, Fused Deposition Modeling, Direct Ink Writing, Photopolymer Inkjet Technologies and Photonic Curing and Robotic Pick and Place technologies. And Chapter 3 presents some demonstrations of possible applications of H3D printing.

5.1 Contributions

What has been accomplished in this thesis is the foundational work required to bring Hybrid 3D Printing from idea to reality. Before this work, there was limited work in H3D printing as printing platforms like the one presented here did not exist. The development of this platform enables the use of multiple AM technologies within a single integrated environment, which has not been done before. The results from the study of the DuPont ME603 silver ink has provided guidelines for curing parameters that are dependent on the intended applications. The silver ink can now be cured in various ways, straying from the manufacturers recommended conditions, to tailor the electromechanical properties. And

most importantly, this work provides a platform to groups of various interests to develop collaborations and help push AM to greater heights.

5.2 Future Work

The potential future work that follows this thesis can cover many research areas. The open architecture, from the software programming to the modular hardware, opens doors to many new avenues. Potential areas of future work include, design for manufacturing with H3D printing, new printing software and printing schemes, material compatibility, functionally gradient materials, printed and embedded electronics to name a few. The platform opens new challenges and areas of innovation along with the whole workflow as a machine of this magnitude has never been presented to the masses and will hopefully provide many opportunities for new research and advancements.

REFERENCES

1. Tibbits, S., *Platform Printers.* 3D Printing and Additive Manufacturing, 2017. **4**(2): p. 61-61.

2. David, E., et al., *Multi-material, multi-technology FDM: exploring build process variations.* Rapid Prototyping Journal, 2014. **20**(3): p. 236-244.

3. Choi, J.-W., E. MacDonald, and R. Wicker, *Multi-material microstereolithography.* The International Journal of Advanced Manufacturing Technology, 2010. **49**(5): p. 543-551.

4. Wicker, R.B. and E.W. MacDonald, *Multi-material, multi-technology stereolithography.* Virtual and Physical Prototyping, 2012. **7**(3): p. 181-194.

5. Amit Joe, L., M. Eric, and B.W. Ryan, *Integrating stereolithography and direct print technologies for 3D structural electronics fabrication.* Rapid Prototyping Journal, 2012. **18**(2): p. 129-143.

6. Raza, I., L. Iannucci, and P.T. Curtis, *Introducing a Multimaterial Printer for the Deposition of Low Melting Point Alloys, Elastomer, and Ultraviolet Curable Resin.* 3D Printing and Additive Manufacturing, 2017. **4**(2): p. 83-89.

7. Crump, S.S., *Apparatus and method for creating three-dimensional objects*. 1992, Google Patents.

8. Renn, M.J., et al., *Apparatuses and methods for maskless mesoscale material deposition*. 2009, Google Patents.

9. Renn, M.J., *Direct write™ system*. 2007, Google Patents.

10. Taibur, R., et al., *Aerosol based direct-write micro-additive fabrication method for sub-mm 3D metal-dielectric structures.* Journal of Micromechanics and Microengineering, 2015. **25**(10): p. 107002.

11. Jones, C.S., et al., *Aerosol-jet-printed, high-speed, flexible thin-film transistor made using single-walled carbon nanotube solution.* Microelectronic Engineering, 2010. **87**(3): p. 434-437.

12. Paulsen, J.A., et al. *Printing conformal electronics on 3D structures with Aerosol Jet technology*. in *2012 Future of Instrumentation International Workshop (FIIW) Proceedings*. 2012.

13. Agarwala, M.K., et al., *Structural quality of parts processed by fused deposition.* Rapid Prototyping Journal, 1996. **2**(4): p. 4-19.

14. Bellini, A., S. Guceri, and M. Bertoldi, *Liquefier Dynamics in Fused Deposition.* Journal of Manufacturing Science and Engineering, 2004. **Vol.126 Issue.2**: p. 237-246.

15. Quanyi, M., et al., *Thermal cure effects on electromechanical properties of conductive wires by direct ink write for 4D printing and soft machines.* Smart Materials and Structures, 2017. **26**(4): p. 045008.

16. Ge, Q., H.J. Qi, and M.L. Dunn, *Active materials by four-dimension printing.* Applied Physics Letters, 2013. **103**(13): p. 131901.

17. Ge, Q., et al., *Active origami by 4D printing.* Smart Materials and Structures, 2014. **23**(9): p. 094007.

18. Yu, K., et al., *Controlled Sequential Shape Changing Components by 3D Printing of Shape Memory Polymer Multimaterials.* Procedia IUTAM, 2015. **12**: p. 193-203.

19. Mao, Y., et al., *Sequential Self-Folding Structures by 3D Printed Digital Shape Memory Polymers.* Scientific Reports, 2015. **5**: p. 13616.

20. Mao, Y., et al., *3D printed reversible shape changing components with stimuli responsive materials.* Scientific reports, 2016. **6**.

21. Wu, J., et al., *Multi-shape active composites by 3D printing of digital shape memory polymers.* Scientific Reports, 2016. **6**: p. 24224.

22. Kim, D. and J. Moon, *Highly conductive ink jet printed films of nanosilver particles for printable electronics.* Electrochemical and Solid-State Letters, 2005. **8**(11): p. J30-J33.

23. Barroso-Bogeat, A., et al., *Temperature dependence of the electrical conductivity of activated carbons prepared from vine shoots by physical and chemical activation methods.* Microporous and Mesoporous Materials, 2015. **209**: p. 90-98.

24. Miyamoto, T. and K. Shibayama, *Free-volume model for ionic conductivity in polymers.* Journal of Applied Physics, 1973. **44**(12): p. 5372-5376.

25. Huang, H. and F. Spaepen, *Tensile testing of free-standing Cu, Ag and Al thin films and Ag/Cu multilayers.* Acta Materialia, 2000. **48**(12): p. 3261-3269.

26. Kim, I., et al., *Effect of microstructural development on mechanical and electrical properties of inkjet-printed Ag films.* Journal of electronic materials, 2008. **37**(12): p. 1863-1868.

27. Lacour, S.P., et al., *Mechanisms of reversible stretchability of thin metal films on elastomeric substrates.* Applied Physics Letters, 2006. **88**(20): p. 204103.

28. Lu, N., et al., *Metal films on polymer substrates stretched beyond 50%.* Applied Physics Letters, 2007. **91**(22): p. 221909.

29. Li, T., et al., *Stretchability of thin metal films on elastomer substrates.* Applied Physics Letters, 2004. **85**(16): p. 3435-3437.

30. Merilampi, S., et al., *Analysis of electrically conductive silver ink on stretchable substrates under tensile load.* Microelectronics Reliability, 2010. **50**(12): p. 2001-2011.

31. Muth, J.T., et al., *Embedded 3D printing of strain sensors within highly stretchable elastomers.* Advanced Materials, 2014. **26**(36): p. 6307-6312.

32. Sawyer, E.J., et al., *Large increase in stretchability of organic electronic materials by encapsulation.* Extreme Mechanics Letters, 2016. **8**: p. 78-87.

33. Costa, P., S. Ribeiro, and S. Lanceros-Mendez, *Mechanical vs. electrical hysteresis of carbon nanotube/styrene–butadiene–styrene composites and their influence in the electromechanical response.* Composites Science and Technology, 2015. **109**: p. 1-5.

34. Yang, Z.-J., et al., *Detailed investigation on elastoplastic deformation and failure of carbon nanotube fibers by monotonic and cyclic tensile experiments.* Carbon, 2015. **94**: p. 73-78.

35. Tobushi, H., S. Hayashi, and S. Kojima, *Mechanical properties of shape memory polymer of polyurethane series: Basic characteristics of stress-strain-temperature relationship.* JSME international journal. Ser. 1, Solid mechanics, strength of materials, 1992. **35**(3): p. 296-302.

36. Heo, G., et al., *Critical Role of Diels–Adler Adducts to Realise Stretchable Transparent Electrodes Based on Silver Nanowires and Silicone Elastomer.* Scientific reports, 2016. **6**.

37. Gercek, H., *Poisson's ratio values for rocks.* International Journal of Rock Mechanics and Mining Sciences, 2007. **44**(1): p. 1-13.

38. Laschi, C., B. Mazzolai, and M. Cianchetti, *Soft robotics: Technologies and systems pushing the boundaries of robot abilities.* Science Robotics, 2016. **1**(1).

39. Trivedi, D., et al., *Soft robotics: Biological inspiration, state of the art, and future research.* Applied Bionics and Biomechanics, 2008. **5**(3): p. 99-117.

40. Mosadegh, B., et al., *Pneumatic Networks for Soft Robotics that Actuate Rapidly.* Advanced Functional Materials, 2014. **24**(15): p. 2163-2170.

41. Ge, Q., et al., *Multimaterial 4D Printing with Tailorable Shape Memory Polymers.* Scientific Reports, 2016. **6**: p. 31110.

42. Ostfeld, A.E., et al., *Screen printed passive components for flexible power electronics.* Scientific Reports, 2015. **5**: p. 15959.